**UNIVERSITY OF THESSALY**

**SCHOOL OF ENGINEERING**

**DEPARTMENT OF MECHANICAL ENGINEERING**


Diploma Thesis

# Evaluation of Pitting Corrosion behavior of 2707 Hyper-Duplex Stainless Steel

By

Alexandra Faka

Supervisor

Dr. Anna Zervaki

Submitted for the Partial Fulfillment of the requirements for the degree of Diploma in Mechanical Engineering

2019


UNIVERSITY OF
THESSALY

## Certified by the members of the Thesis Committee:

First examiner (Supervisor)
Dr. Anna Zervaki
Lab Teaching Staff,
Department of Mechanical Engineering,
University of Thessaly

Second examiner (Co-Supervisor)
Dr. Angeliki Lekatou
Professor,
Department of Materials Science and Engineering,
University of Ioannina

Third examiner
Dr. Alexios Kermanidis
Assistant Professor,
Department of Mechanical Engineering,
University of Thessaly

# Acknowledgments

This project is accomplished in the scope of partial fulfilment of the requirement of degree of Diploma in Mechanical Engineering at University of Thessaly.

For the successful outcome of this Thesis, I would like to express my sincere gratitude to my Thesis' supervisors, Dr. Anna Zervaki and Professor Angeliki Lekatou for the continuous support of my research, their guidance helped me to overcome any difficulty during the composition of this study. Without their guidance and persistent help this Thesis would not have been possible.

Furthermore, very special thanks for to Assistant Professor Alexios Kermanidis for accepting to be the referee of this study.

My sincere thanks also goes to Dr. Spyros Kleftakis from the laboratory of Applied Metallurgy at University of Ioannina for the crucial support during the conduction of cyclic potentiodynamic polarization test and the critical pitting temperature tests. Without his participation and input, the survey could not have been successfully conducted.

In addition, I would like to express my very great appreciation to Dr. Gkolia Evaggelia from University of Thessaly from the Department of Agriculture Crop Production and Rural Environment for the conduction of AAS.

I would also like to express my gratitude to Professor Helen Pavlidou from the Aristotle University of Thessaloniki for the conduction of SEM/EDX analyses.

Also, I would like to thank Professor George Vourlias and PhD Candidate Dimitrios Karfaridis for the conduction of the XPS analyses.

Last but not least, a special thanks to my family and friends. Words cannot express how grateful I am to them for all their sacrifices, their encouragement and patience during all my college years and especially during this study.

# Abstract

Hyper-duplex stainless steels have raised the scientific community's interest due to their exceptional properties of the characteristic two-phase microstructure (50% ferrite and 50% austenite). More specifically, their microstructure offers them higher corrosion resistance in chloride environments and higher mechanical properties than the other common steels. These advantages make HDSS suitable for aggressive, acidic and/or chloride process environments that exist in various industries, such as petroleum, gas refineries and marine environments. Thus, this thesis focuses on the study of the behavior of hyper-duplex stainless steel 2707 in chloride environment and its susceptibility to pitting corrosion, as well as the determination of the critical pitting temperature.

In order to define the properties of pitting susceptibility, cyclic potentiodynamic polarization test (CPP) was conducted in 3,5% wt. NaCl solution, which represents sea water. For the measurement of the critical pitting temperature (CPT), potentiostatic polarization at a 5% wt NaCl solution was used. Both tests were performed in the Department of Materials Science at the University of Ioannina. The specimens, both the curves and hollows, were properly prepared at the University of Thessaly where they were examined after the tests. For the examination and the evaluation of the pitting corrosion, Stereo-Optical microscopy, SEM, EDX, AAS and XPS analyses were conducted.

In addition, by the analysis of the cyclic potentiodynamic polarization curves gave information about the behavior of the alloy in the selected environment and the corrosion rate was calculated. The corrosion mechanism and its products have been identified in those conditions. Also, a comparison of the results of two different condition test was made and the influence of the open circuit equilibrium time on the pitting corrosion was established. Finally, the critical pitting temperature was determined by the potentiostatic polarization test.

Finally, the results of this study highlight the characteristics of hyper-duplex stainless steel and its susceptibility to pitting corrosion, confirming its exceptional properties, its significance in the field of material science as well as the need for further exploration of its possibilities.

# Περίληψη

Οι υπερ-διφασικοί ανοξείδωτοι χάλυβες έχουν κεντρίσει το ενδιαφέρον της επιστημονικής κοινότητας λόγω τον εξαιρετικών ιδιοτήτων που τους προσφέρει η χαρακτηριστική μικροδομή τους που αποτελείται από ίσες ποσότητες φερρίτη και ωστενίτη. Πιο συγκεκριμένα, η μικροδομή τους τους προσφέρει υψηλότερη αντίσταση στην διάβρωση σε χλωριούχα περιβάλλοντα και υψηλότερες μηχανικές ιδιότητες από τους υπόλοιπους κοινούς χάλυβες, κάνοντάς τους κατάλληλους για χρήση σε επιθετικά, όξινα ή/και χλωριούχα περιβάλλοντα που υπάρχουν στην βιομηχανία όπως στα διυλιστήρια πετρελαίου, αερίου και σε θαλασσινά περιβάλλοντα. Έτσι, η έρευνα αυτή εστιάζει στην μελέτη της συμπεριφοράς του υπερ-διφασικού ανοξείδωτου χάλυβα 2707 σε χλωριούχο περιβάλλον και πιο συγκεκριμένα στην επιδεκτικότητά του στην τρημματική διάβρωση, όπως επίσης και στην εύρεση της κρίσιμης θερμοκρασίας που ξεκινά η διάβρωση αυτή.

Για την εύρεση αυτών τον ιδιοτήτων έγιναν κυκλικές ποτενσιοδυναμικές πολώσεις (CPP) σε 3.5 % κβ. NaCl διάλυμα, που προσμοιάζει το θαλασσινό νερό, ενώ για την κρίσιμη θερμοκρασία τρημματικής διάβρωσης διεξήχθη ποτενσιοστατική πόλωση (CPT) σε 5 % κβ. NaCl διάλυμα. Και οι δύο πειραματικές διαδικασίες διεξήχθησαν στο Τμήμα Επιστήμης Υλικών του Πανεπιστημίου Ιωαννίνων. Τα δείγματα, τόσο τα κοίλα όσο και τα κυρτά, προετοιμάστηκαν στο Πανεπιστήμιο Θεσσαλίας, όπου και εξετάστηκαν μετά το πέρας των πειραμάτων. Για την αξιολόγηση της τρημματικής διάβρωσης πραγματοποιήθηκαν στερεοσκοπική και μικροσκοπική παρατήρηση, καθώς επίσης αναλύσεις SEM, EDX, ατομική απορρόφηση και XPS.

Στην συνέχεια, από την ανάλυση των καμπυλών των κυκλικών ποτενσιοδυναμικών πολώσεων παρουσιάστηκε με ακρίβεια η συμπεριφορά του συγκεκριμένου χάλυβα στο επιθυμητό διαβρωτικό περιβάλλον καθώς επίσης υπολογίστηκε και ο ρυθμός διάβρωσης. Επίσης ταυτοποιήθηκαν ο μηχανισμός και τα προϊόντα διάβρωσης αλλά και έγινε η σύγκριση των αποτελεσμάτων των κυκλικών ποτενσιοδυναμικών πολώσεων που έγιναν έπειτα από μία και δύο ώρες ισορροπίας ανοιχτού κυκλώματος. Τέλος, μέσω των καμπυλών της ποτενσιοστατικής πόλωσης καθορίστηκε η κρίσιμη θερμοκρασία.

Τέλος, μέσα από τα αποτελέσματα της έρευνας αυτής επισημαίνονται τα χαρακτηριστικά του υπέρ-διφασικού ανοξείδωτου χάλυβα και της επιδεκτικότητάς του στην τρημματική διάβρωση επιβεβαιώνοντας τις εξαιρετικές ιδιότητες του, την σημαντικότητα του στον τομέα της επιστήμης των υλικών όπως επίσης και την ανάγκη για περεταίρω διερεύνηση των δυνατοτήτων του.

# Table of Contents

# List of Figures

# List of tables

# Chapter 1: Introduction

## 1.1 Aim and Structure of the Diploma Thesis

The current diploma thesis focuses on the pitting corrosion behaviour of the hyper- duplex stainless steel 2707, by means of cyclic potentiodynamic polarization in 3,5% NaCl solution in 1-hour open circuit equilibrium time. In parallel the Critical Pitting Temperature (CPT) of the steel, through potentiostatic measurements in 5% NaCl solution was also determined.

The current thesis continues the work started one year earlier by K.Karagiannis [1], where cyclic potentiodynamic polarization tests were conducted after 2-hours open-circuit equilibrium time. The whole thesis composes of five chapters which are briefly presented below.

In the 1st Chapter-besides the aim- a brief introduction on the pitting corrosion phenomena is provided.

In the 2nd Chapter, the literature review is presented. The characteristics of the hyper-duplex stainless steel (HDSS) 2707, are described alongside its properties and microstructural characteristics in order to highlight its superiority in comparison to other alloys.

In the 3rd Chapter, the experimental procedure is given. The experiments conducted included Cyclic potentiodynamic polarization test (CPPT) and Critical pitting temperature tests (CPT).

In the 4th Chapter, the cyclic potentiodynamic polarization curves are interpreted in order to reach in conclusions about the behavior of HDSS 2707 in selected corrosive environment. Atomic absorption spectrometry method analysis of the NaCl solution collected after the CPP experiments, optical and stereo microscopy studies and SEM/EDX and XPS analyses are presented. There is the determination of the critical pitting temperature.

In the 5th Chapter, the results are discussed in order to define the resistance of the super-duplex steel 2707 against pitting corrosion, to describe the corrosion mechanism and also conclude the effect of the time of open circuit equilibrium time. In the end, some future work recommendations are provided.

The flow diagram is presented below:

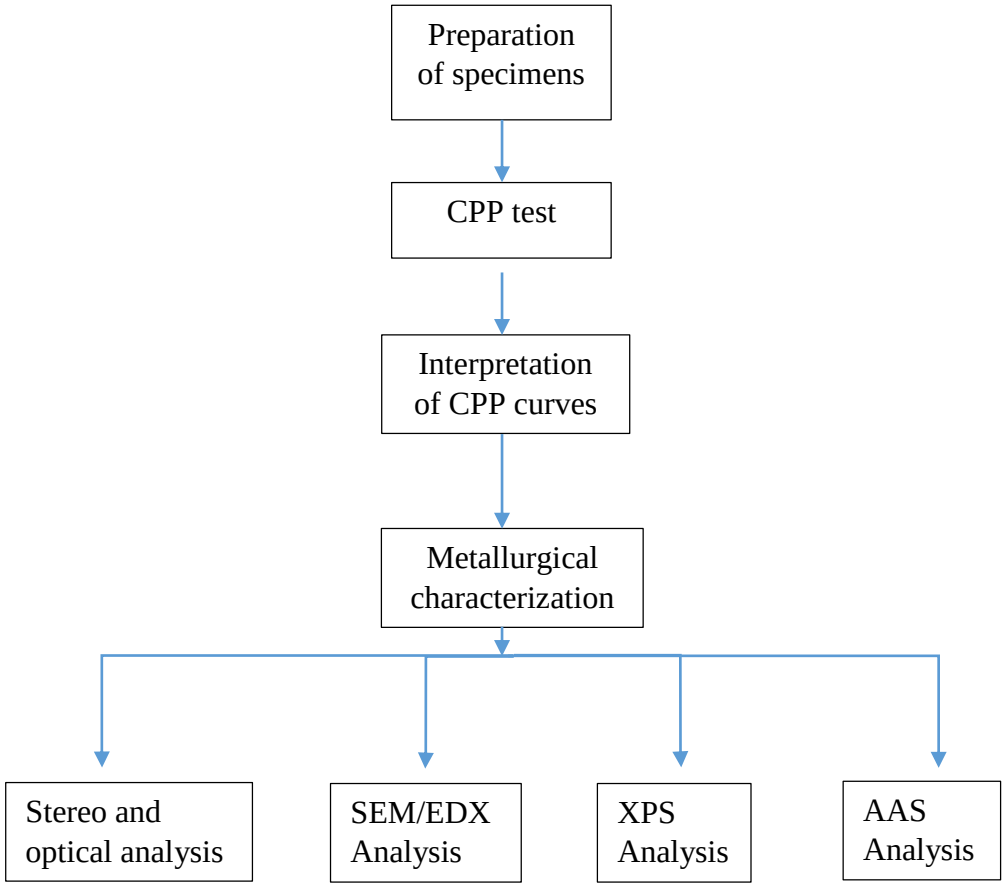
Preparation of specimens
CPP test
Interpretation of CPP curves
Metallurgical characterization
Stereo and optical analysis
SEM/EDX Analysis
XPS Analysis
AAS Analysis

## 1.2 Corrosion in metals

Corrosion is defined as the destruction or deterioration of a material because of reaction with its environment. The understanding of corrosion is important for three main reasons: safety, economics and conservation. This is the reason why many studies have been made to deepen the understanding of the causes of corrosion and the ways to prevent or at least minimize damage caused by corrosion. [2][3]

## Electrochemistry of corrosion

A metal immersed in a conducting solution will undergo two distinct reactions which proceed simultaneously on the metal surface:

i) The anodic reaction: $M \rightarrow M^{n+} + ne^-$ (oxidation) (1.1)

ii) The cathodic reaction:

$$2H_2O + O_2 + 4e^- \rightarrow 4OH^- \quad \text{or} \quad 2H^+ + 2e^- \rightarrow H_2 \text{ (reduction)} \qquad (1.2)$$

depending on the type of electrolytic solution, neutral or acid respectively.

iii) The total reaction of oxidation and reduction is (redox):

$$2M + 2H_2O + 0_2 \rightarrow 2M(0H)_2 \text{ (neutral)} \quad \textit{or} \quad M + 2H^+ \rightarrow H_2 + M^{2+} \text{ (acid)} \qquad (1.3)$$

where M is a divalent metal. [2][4]

The electrons lost in an oxidation component are gained in a reduction component enabling electroneutrality to be maintained. These simultaneous reactions occur at a single potential, the corrosion potential ($E_{corr}$). The corrosion potential depends on the combination both of the anodic and cathodic reactions and the oxidation state of the metal depends on this potential. The coupling of the corroding material and the solution can be considered as a galvanic cell in which energy diffuses by the consumption of the oxidant.
Corrosion is a surface reaction that begins from the surface's defaults such as cracks and inclusions where the atoms have high energy. The atoms try to reduce the energy by participating in chemical reactions. Finally, the corrosion spread to all over the surface and beneath the surface of the metal. [5][6]

## Polarization

For every electrochemical reaction, there is an equilibrium electrode potential, $E_q$ and the metal's potential in relation to the equilibrium potential, E. If $E>E_q$, the reaction leads to the direction of oxidation, but if $E<E_q$, the reaction proceeds in the direction of reduction, e.g. metal deposition. When corrosion occurs, the deviation from the steady state due to the passage of current is known as polarization which affects the corrosion rate. [4]

## 1.3 Types of corrosion

The different types of corrosion are: (Fig. 1) [1][3][7]

- Uniform corrosion: uniform corrosion develops uniformly on the surface of the material and is accompanied by generalized reduction of thickness to failure.it is characterized as the most important form of corrosion.
- Pitting corrosion: localized corrosion, more dangerous than uniform corrosion. Pits are formed on the surface of the material. This type of corrosion is due to specific corrosive environments that are often different from the general operating environment. Pitting corrosion leads to local reduction in thickness, concentrations and cracks are beginning to form.
- Crevice corrosion: a localized form of corrosion that is developed in stationary solutions in slits and recesses. The obstruction of oxygen diffusion into the recess creates an electrolytic cell with deferent concentration. The recess region is an anode. The presence of chlorides transforms turns the recess environment into an extremely acidic environment with intense corrosive action.
- Galvanic corrosion: this type of corrosion takes place when two dissimilar metals come into contact in the presence of an electrolyte and is due to the potential difference between the two metals. Therefore, one of the two metals acts as anode and erode, while the other acts as cathode an is protected.
- Selective leaching: this type of corrosion has as result the removal of an alloy element from a metal alloy.
- Cavitation: is due to a liquid or gas and is caused by impact stress on the surface of the metal, which can cause sensitivity, fatigue, even local detachment of material and formation of pits. Cavitation often acts with other types of corrosion, such as galvanic corrosion.
- Erosion corrosion: is caused by electrochemical reaction simultaneous with mechanical action due to the relative movement between the electrolyte and the surface of the metal.
- Stress corrosion cracking: is because of the combination of tensile stress and corrosive environment. The tensile stress may be an externally applied stress or a remained stress from a specific process or welding. Stress corrosion cracking usually occurs in specific material-voltage-environment combinations, it is characterized by the propagation of cracks in the material, which can be detected only by microscopic control.
- Intergranular corrosion: Stainless steels and weld decay sensitization are the best examples of intergranular corrosion. Grain boundaries that are rich in chromium

elements will precipitate lead. Carbon and chromium can be combined and form chromium carbides at specific temperatures and make the grain boundaries vulnerable.

- Hydrogen embrittlement: is a form of brittleness due to the introduction and trapping of hydrogen in the material. The reaction of the water during a corrosive action is an important source of hydrogen. High strength materials are more susceptible to hydrogen embrittlement than lower strength materials.

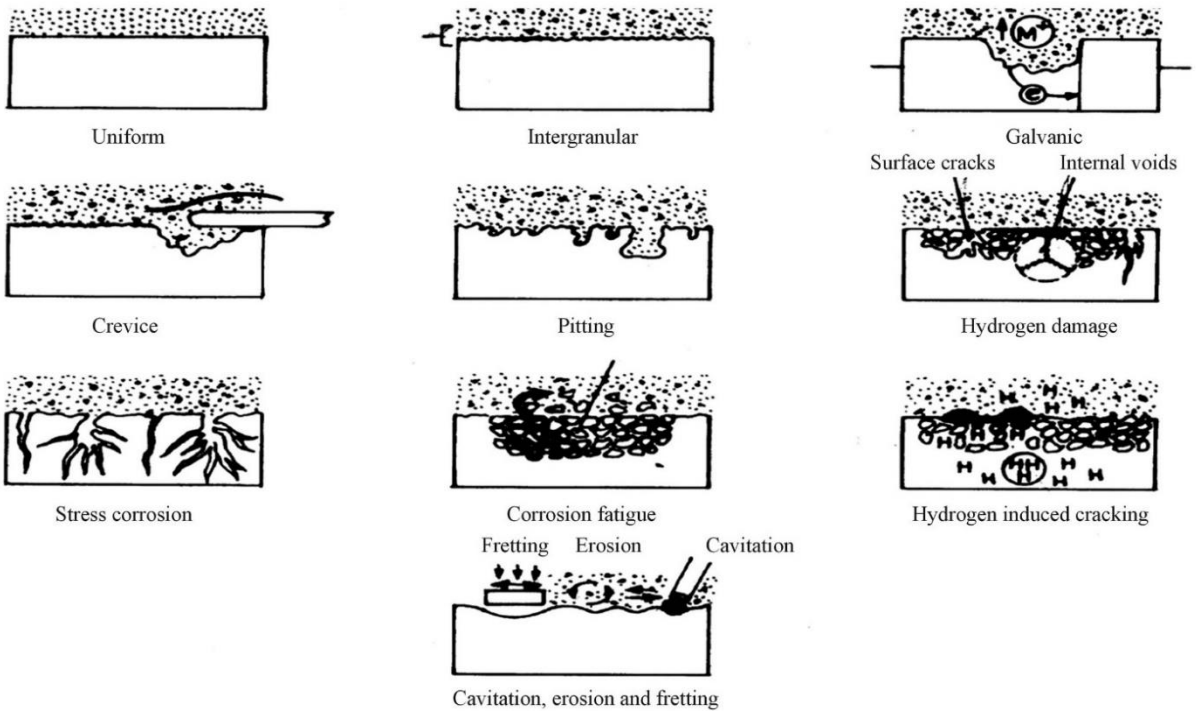


**Fig.1**: Types of corrosion.[3]

This thesis investigates the pitting corrosion and its characteristics because it is considered as one of the most dangerous and intense forms of corrosion. The small, difficult to detect, pits can cause equipment failure with only a small percent weight loss of the entire structure. Furthermore, it is difficult to interpret the extend of the pitting due to its variation on depth and density of pits that may occur under identical conditions. [3]

## 1.4 Pitting corrosion

### 1.4.1 Mechanism of pitting corrosion

Pitting corrosion is a localized corrosion because of the dissolution of the protective passive layer on the surface of the metal. The process of pitting involves the breakdown of the passive film, the formation of metastable pits and their growth. When the protective passive film starts to be dissolved the electrolyte gradually acidify due to its inadequate aeration, this leads the pH of the pits to increase by increasing the anion concentration. [2][8]

More specifically, an electrolyte rich in chloride and/or sulfides attack to the protective passive layer of the stainless steel and start to dissolve it. The protective film is composed by $Cr_2O_3$ and when anions and a proper voltage applied, the film breaks. The voltage is known as pitting voltage. (Fig.2) After the breakdown of the passive film, pits begin to form and the anion concentration ($Cl^-$) in the electrolyte increase leading to pits growing further. Sometimes, the corrosion resistance of stainless steel recovered partially by repassivation of the pits. The most common reactions responsible for the corrosion in stainless steel at NaCl solution are: (Fig.3)

Anodic reaction: $Fe \rightarrow Fe^{2+} + 2e^-$ (dissolution of iron) (1.4)

$$Fe^{2+} + 2H_2O \rightarrow FeOH^+ + H_3O^+ \quad (1.5)$$

($FeOH^+$ is mainly responsible for the current increasing)

Cathodic reaction: $O_2 + 2H_2O + 4e^- \rightarrow 4OH^-$ (1.6)

Total reaction: $Fe^{2+} + 2Cl^- \rightarrow FeCl_2$ (1.7)

$$FeCl_2 + 2H_2O \rightarrow Fe(OH)_2 + 2HCl \quad (1.8)$$

($Fe(OH)_2$ is responsible for the Ph increasing inside the pit leading to further corrosion)

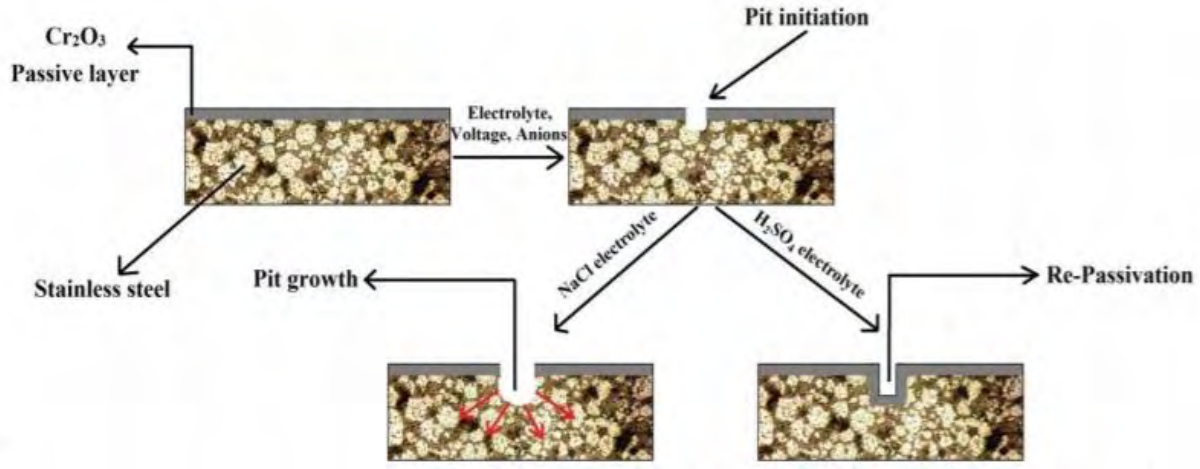


**Fig. 2**: Mechanism of pitting corrosion [8]

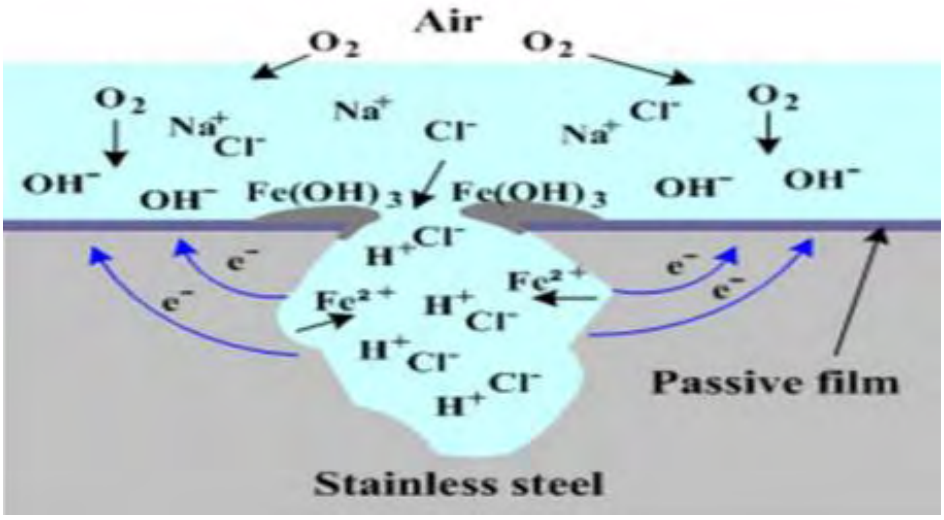


**Fig 3**: Electrochemistry reaction of pitting corrosion. [9]

## 1.4.2. Types of pitting corrosion

Pits vary about their sizes and shapes. A visual examination of the exposed surface of the metals may give significant information about the pits, such us their number, but not so accurate about the actual characteristics of pits that are under the surface. For this, a cross-section examination can be useful to determine the accurate shape and depth of the pits. Different shapes of pits are demonstrated in figure 4.[10]

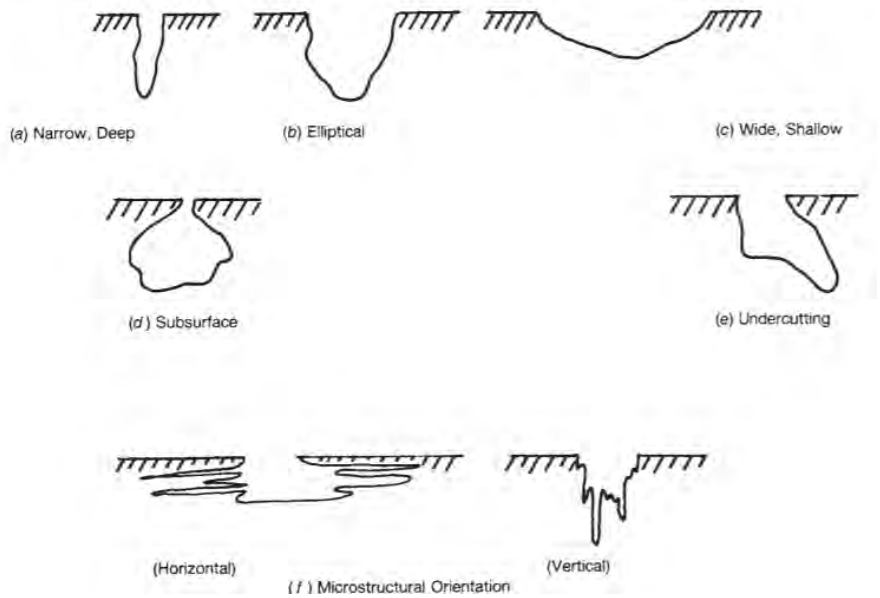


**Fig. 4**: Variation in the cross-sectional shape of the pits. [10]

### 1.4.3 Evaluation of pitting corrosion

The life of the material can be predicted from the evaluation of the pitting. Many methods have been suggested for the evaluation of the pitting and it is preferable for more accurate characterization to employ at least two of them. [10]
The main methods that are referred in the literature are:

- **Standard charts**: Rank the pits in terms of density, size, and depth on the basis of standard charts, such as those shown in figure 4. Columns A and B are related to the surface of the metal and Column C is related to the depth of the pits. A typical rating might be A-3, B-2, C-3, representing a density of 5 x $10^4$ pits/$m^2$, an average pit opening of 2.0 $mm^2$, and an average pit depth of 1.6 mm.

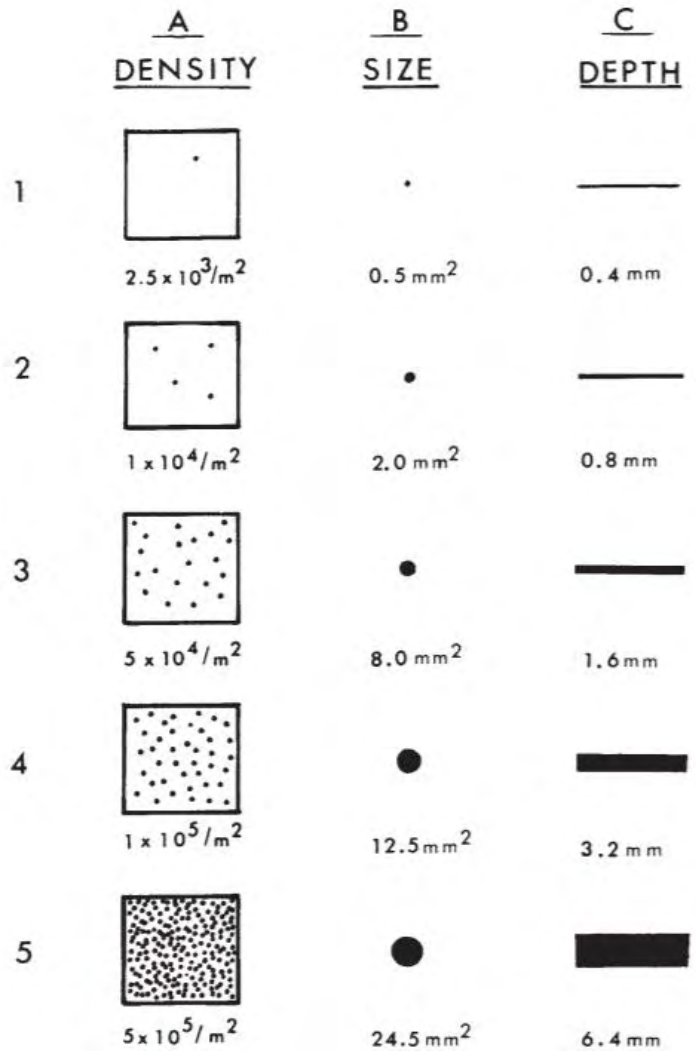


**Fig. 5**: Standard rating charts for pits. [10]

- **Metal Penetration**: determine the deepest pits and express metal penetration in terms of the maximum depth or the average of the deepest pits. This method is useful when the metal is used for the storage of a gas or liquid, and a hole could lead to a loss of fluid. Metal penetration can be expressed as pitting factor.

$$Pitting\ factor = \frac{deepest\ metal\ penetration}{average\ metal\ penetration}\ , \qquad (1.9)$$

If PF = 1 then uniform corrosion exists. The larger the PF, the greater the depth of penetration. This method is not accurate in cases if pitting or general corrosion is negligible

- **Statistical**: Many factors can contribute to the formation and distribution of pits such us tendency of the metal to corrode, environment, exposed area and time of the exposure. The pitting probability test can only provide information about the susceptibility of metals to pitting corrosion and not to the rate of spreading.

$$P = \frac{N_p}{N} \cdot 100 \qquad (1.10)$$

where:
P (%): pitting probability
$N_p$: number of specimens exhibiting pitting corrosion
N: total number of specimens.

- **Loss in mechanical properties**: When pitting corrosion is the main form of corrosion and the number of the pits per area is high, deterioration of mechanical properties (tensile strength, elongation, fatigue strength, etc.) can be used to determine the magnitude of the pitting corrosion.

## 1.5 Electrochemical techniques

Electrochemical techniques are used to determine the corrosion rate and the pitting potential. In contrast, techniques such as systematic recording of the weight loss require long exposure times to measure corrosion rate reliable.

### 1.5.1. Tafel Extrapolation

Tafel extrapolation is an electrochemical technique to estimate either the corrosion current ($i_{corr}$) or the corrosion potential ($E_{corr}$) in an electrochemical cell, and by extension, the corrosion rate. This method uses data from cathodic and anodic polarization measurements. Extrapolation is performed by extending the linear portions of the anodic and cathodic plots to their intersection (Fig.6). At the intersection point, the corrosion current $i_{corr}$, can be obtained. [1][2][11][12]

The anodic and cathodic Tafel plots are described by the Tafel equations:

$$\log i = \log i_{corr} + \frac{E - E_{corr}}{B_a} \quad \text{(anodic oxidation curve)} \qquad (1.11)$$

$$\log |-i| = \log i_{corr} + \frac{E_{corr} - E}{B_c} \quad \text{(cathodic reduction curve)} \qquad (1.12)$$

Where,
$B_{a,c}$ =Tafel slope
$i_{corr}$ = corrosion current density in μA/cm$^2$
i= current density in μA/cm$^2$
$E_{corr}$ = corrosion potential in mV
E= potential in mV

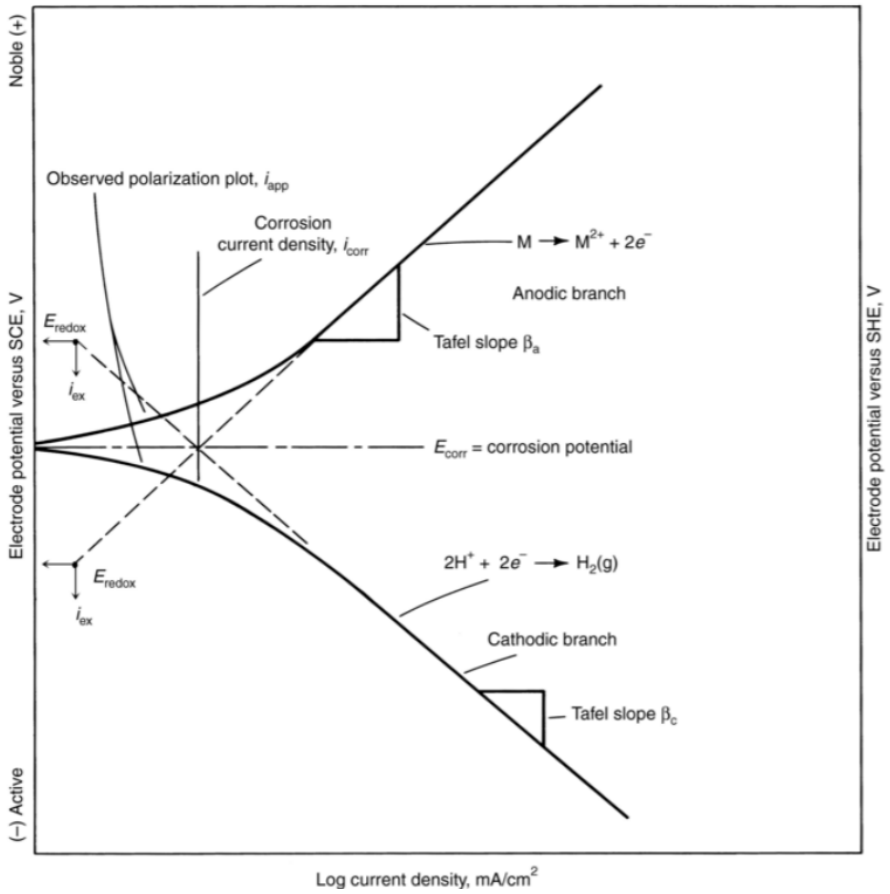


**Fig. 6**: Tafel diagram. [11]

## 1.5.2. Corrosion rate expressed as penetration rate

Faraday's Law is used to determine weight loss via $i_{corr}$, according to the following expression:

$$W = \frac{I \cdot t \cdot M}{n \cdot F} \qquad (1.13)$$

where, W: weight loss (gr),
I: current (μA/cm$^2$),
t: time (sec),
n: number of electrons
F: Faraday's constant (96.487 C/gr-equivalent)
M: molecular weight of the electroactive species.

The rearrangement of the above equation gives the corrosion rate:

$$\text{CR} = K \cdot \left(\frac{i_{corr}}{d}\right) \cdot EW \qquad (1.14)$$

where:
CR: corrosion rate (in mm per year)
K: conversion coefficient, K= 3,27 × 10$^3$ (when $i_{corr}$ is expressed as μA/cm$^2$).
$i_{corr}$: corrosion current density (mA/cm$^2$)
d: alloy density (g/cm$^3$) (d2707 = 7,8061 g/cm$^3$)
EW: equivalent weight of the alloy in gr

**Table 1:** Values of conversion coefficient

| CR | $i_{corr}$ | d | K | K |
|---|---|---|---|---|
| mpy | μA·cm$^{-2}$ | g·cm$^{-3}$ | 0,1288 | mpy g/(μA·cm) |
| mm·yr$^{-1}$(1) | A·m$^{-2}$ | kg·m$^{-3}$ | 327,2 | mm Kg/(A ·m y) |
| mm·yr$^{-1}$(2) | μA·cm$^{-2}$ | g·cm$^{-3}$ | 3,27·10$^{-3}$ | mm g/(μA·cm y) |

For alloys, the EW is calculated according to ASTM G102:

$$EW = \frac{1}{\Sigma(\frac{n_i \cdot f_i}{AW_i})} \qquad (1.15)$$

Where $f_i$: mass fraction of the i$^{th}$ component of the alloy
$AW_i$: the atomic weight of the i$^{th}$ component element (g/mol)
$n_i$: is the number of electrons transferred or lost when oxidizing the i$^{th}$ component element under the conditions of the corrosion process (equivalents/mol)
i: the number of component elements in the alloy

Table 2 contains information for HDSS 2707.

**Table 2:** Elements' info for the calculation of EW.

| Alloying element | Degree of ionization (ni) | Weight percentage (%) | Atomic weight (g/mol) |
|---|---|---|---|
| Fe | +2 | 58,225 | 55,845 |
| Mn | +2 | 1,5 | 54,938 |
| Cr | +3 | 27 | 51,9961 |
| Ni | +2 | 6,5 | 58,6934 |
| Mo | +4 | 4,8 | 95,94 |
| Co | +2 | 1 | 58,933 |

Substituting the above values in equation (1.15)

$$EW_{2707} = 24,07 \qquad (1.16)$$

The above equations can be used when all the elements oxidized with uniform rate during corrosion. [1][11][12]

# Chapter 2: Literature Review

## 2.1 Duplex stainless steels

Duplex stainless steels (DSS) are used in various industries as they combine excellent mechanical properties and corrosion resistance. Duplex stainless steels are alloys which contain nearly equal amounts of the ferrite and austenite phases in their microstructure. Generally, the amounts of ferrite and austenite phases depend on the chemical composition of the alloy and the heat treatment. The ferrite-austenite steels exhibit superior mechanical properties in comparison to the precursor ferritic or austenitic families as demonstrated in Table 3.[13]

**Table 3:** Basic chemical composition, and mechanical properties of three types of stainless steel.

| Structure | C | Cr | Ni | Short name | 0,2%YS $R_{p0,2}$,(MPa) | UTS $R_{pm}$(MPa) | J(Aν) | %E $A_5$(%) |
|---|---|---|---|---|---|---|---|---|
| Ferrite | <0,1 | 13-30 | <0,1 | X8Cr18 | 345 | 540 | - | 20 |
| Austenite | <0,1 | 17-26 | 7-26 | X5CrNi18-10 | 190 | 450 | >100 | 45 |
| Duplex | <0,1/0,4 | 24-28 | 4-7 | X2CrNiMoN22-5-3 | 450 | 700 | >100 | 25 |

The advantages and disadvantages of duplex steels, compared to single-phased ferritic- and austenitic alloys are given in Table 4.

**Table 4:** Advantages and Disadvantages of the DSS.

| Advantages | Disadvantages |
|---|---|
| • Higher strength than austenitic steels.<br>• Higher impact value than ferritic steels.<br>• Increased resistance against general corrosion.<br>• Increased resistance against intergranular, pitting, crevice corrosion, and stress-corrosion cracking.<br>• Higher resistance against hydrogen embrittlement than ferrites.<br>• Better thermal conductivity than austenitic steels. | • Complex precipitation and transformation behavior.<br>• High tendency to embrittlement due to formation of carbides, nitrides, and intermetallic phases.<br>• Reduction of the corrosion resistance due to formation of carbides, nitrides, and intermetallic phases.<br>• Advanced knowledge is needed for the production of components. |

Different types of DSS are containing significant amounts of several alloying elements in order to obtain better mechanical and corrosion properties. Each alloying element has a specific effect on the properties of the steel as is shown in Table 5. [13]

**Table 5:** Influence of alloying elements on microstructure and corrosion resistance of DSS

| Alloying | Effect | Reason | Practical Limitation |
|---|---|---|---|
| C | Negative | Causes precipitation of chromium carbides with accompanying chromium depleted zones | About 0.03% maximum |
| Si | Positive | Si Stabilizes the passive film | About 2% maximum, due to its effect on structural stability and on nitrogen solubility |
| Mn | Negative | Mn-rich sulphides act as initiation sites for pitting. Mn may also destabilize the passive film | About 2%. Higher level may increase the risk of intermetallic precipitation |
| S | Negative | Sulphides if not Cr-Ti or Ce rich, tend to initiate pitting attack | About 0.003%, if maximum pitting resistance required. For reasonable machining, up to 0.02% allowed |
| Cr | Positive | Cr stabilizes the passive film | Between 25 and 28% maximum depending on the Mo content. Higher Cr content increases the risk of intermetallic precipitation |
| Ni | Negative | Increased Ni, other elements constant, dilutes the γ- phase with regard to N, which in turn decreases the PRE of the γ- phase. If the alloy is very sensitive to precipitation of chromium nitrides, Ni can have a positive effect | Ni should primarily be used to give the alloy desired austenite content. |
| Mo | Positive | Mo stabilizes the passive film, either directly or through enrichment beneath the film | About 4-5% depending on the Cr content. Mo enhances the risk of intermetallic precipitation |
| N | Positive | N increases the PREN of the γ phase, not only be increasing the N content of that phase, but also by increasing the Cr and Mo contents through their partitioning coefficients | About 0.15% in Mo free grades. About 0.3% in super duplex and some in 0.4% in 25%Cr, high Mo, high Mn alloys |
| W | Positive | Probably same as Mo | Increases the tendency of intermetallic precipitation |
| Cu | Disputed | Marginal positive and negative effect | About 2.5% maximum. Higher levels reduce hot workability and undesirable hardenability |

## 2.2 PREN value

The DSS are classified in relation to their corrosion resistance according to their pitting resistance equivalent number (PREN):

**Lean duplex ≤ 35 < Duplex < 40 ≤ Super duplex < 45 ≤ Hyper Duplex**

The PREN value for austenitic and duplex stainless steels is given by the following formula:

$$PREN = Cr + 3{,}3Mo + 16N \qquad (2.1)$$

where element content in wt %.

Steels with PREN values over 40 are suitable for use in seawater up to 20 $^{o}$C. However, besides the high PREN values pitting corrosion resistance is also dependent on microstructural features. These include ferrite/austenite proportion, intermetallic precipitates, secondary phases and distribution of specific elements between austenite and ferrite. Partitioning of Cr and Mo in ferrite, and Ni and N in austenite affect the PREN values of both phases resulting thus in selective pitting corrosion of the weakest one. Equal pitting corrosion resistance for both phases are important for the end users, so alloying and heat treatment must be selected properly.

## 2.3 Hyper Duplex Stainless steel (HDSS) 2707

Environmental requirements and raised productivity demands have, in many areas, forced the end-users into recirculation of process streams, with increased temperatures and pressures leading to extremely aggressive environments for the super duplex grades. Therefore, a new hyper duplex stainless steel (HDSS) has been developed for these aggressive conditions, namely SAF 2707HD. [15]

Chemical compositions of the hyper duplex stainless steel grade UNS S32707 alongside similar grades are given in Table 6. Sandvik SAF 3207 HD contains the highest amounts of the alloying elements. The max N content is 0.5 wt%.

**Table 6:** Nominal chemical composition of the HDSS, UNS S32707, S33207 and S32750.

| Commercial name | UNS | C (max) | Cr | Ni | Mo | N | PREN* (min) |
|---|---|---|---|---|---|---|---|
| Sandvik SAF 2507 | S32750 | 0,03 | 25 | 7 | 4 | 0,3 | 42,5 |
| Sandvik SAF 2707 HD | S32707 | 0,03 | 27 | 7 | 5 | 0,4 | 48 |
| Sandvik SAF 3207 HD | S33207 | 0,03 | 31 | 7 | 3,5 | 0,5 | 50 |

SAF 2707 HD (UNS S32707) has a balanced composition, with approximately 50% ferrite and 50% austenite and is designed for use in acidic chloride containing environments. The combination of Cr, Ni and Mo increases resistance to localized corrosion, i.e. pitting and crevice corrosion. The challenge of developing new, highly alloyed DSS by increasing these alloying

elements is to balance the alloying level to control the risk for formation of undesirable intermetallic phase. As indicated in Fig. 7, from 700 to 1080 C$^{o}$, there are sigma phase and chromium nitrides precipitates, besides the austenitic and ferritic phases. [15]

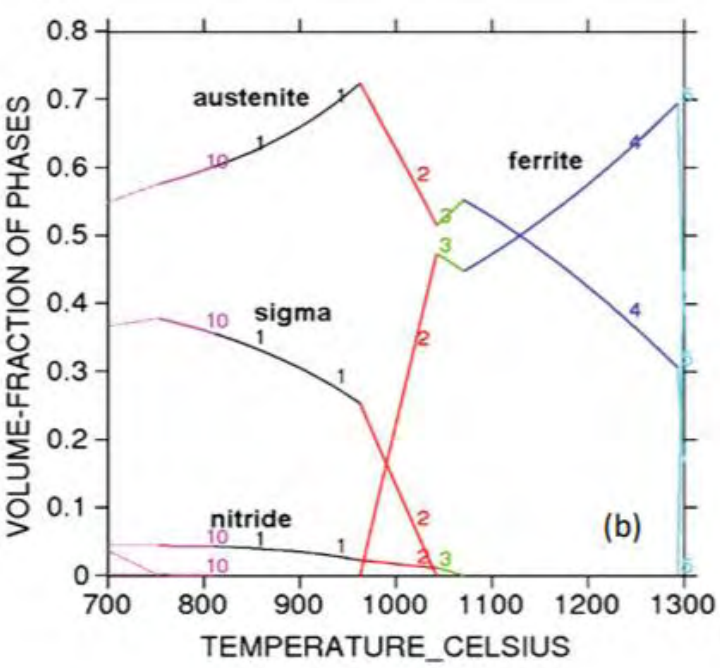


**Fig. 7**: Phase diagram of a hyper duplex stainless steel. [15]

These microstructural changes can occur as a result of improper heat treatments or unsuitable cooling rates, and they are a direct consequence of ferrite instability at high temperatures. The intermetallic phases start forming at austenite-ferrite boundaries, which are nucleation sites characterized by lowest interface energy, and then grow inside ferrite grains, in which diffusion is 100 times faster than in austenite. As these compounds are rich of Cr and Mo, surrounding areas deplete in these elements, and thus remarkably decrease localized corrosion resistance. Furthermore, they have a detrimental effect on ductility and toughness of duplex steels. It is well known that the chemical composition has a fundamental role in the precipitation kinetics. Alloying elements as Cr, Mo, Cu and W promote the precipitation and increase the stability range of intermetallic compounds. Fig. 8 shows the TTT diagram for a typical DSS.

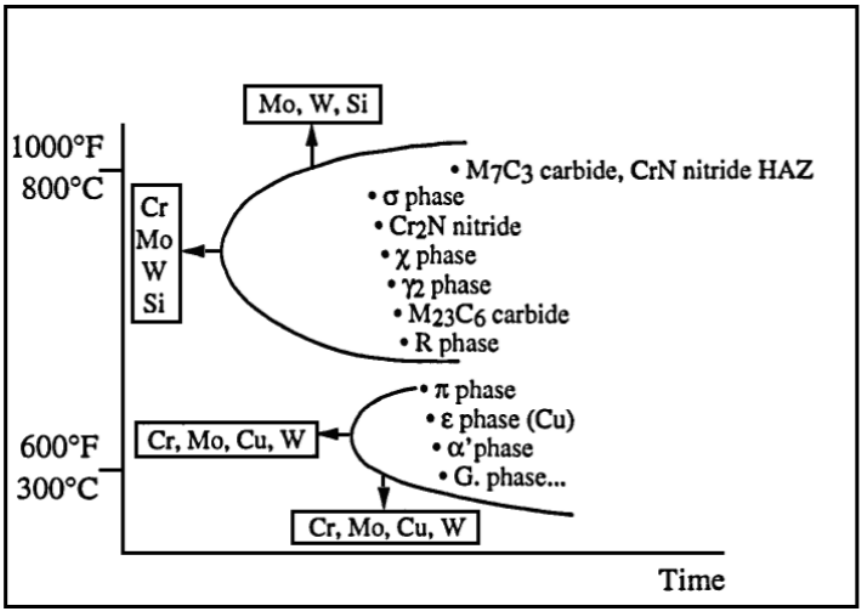


**Fig. 8**: Precipitation reactions which may occur in DSS [18]

As shown in Fig. 8, low temperature range (300-600 ºC) is characterized by the spinoidal decomposition of ferrite in certain domains rich and poor in Cr. Another important transformation in this range concerns G-phase precipitation, an intermetallic compound with general formula $T_6Ni_6Si_7$, where T is a transition element such as Ti, Mn, Cr, Zr, V, Ta, Hf, or Hb. The final result is a remarkable embrittlement of the material, which is the reason why DSS applications are restricted to temperatures lower than 280°C.

Furthermore, at high temperatures (650-1000 ºC) ferrite phase undergoes eutectic transformation and decomposes in sigma phase and secondary austenite. Many other secondary phases may precipitate in this range such as intermetallic compounds, carbides, nitrides. Sigma phase is the most important precipitate (Table 7). The formation of σ is mainly favored by Cr and Mo. The precipitation kinetics and the incubation time are highly affected by the chemical composition of the steel. For this reason, high-alloyed steels like Super/Hyper Duplex are extremely sensitive to these precipitations. The result is remarkable decreasing in both mechanical and corrosion resistance properties.[18]

**Table 7:** Chemical composition of sigma phase (σ).

| Cr | Ni | Mo | W |
|---|---|---|---|
| 29-34 | 3-5 | 3-9 | 0-7 |

### 2.3.1 Corrosion properties

The 2707 HDSS meet the expectations in harsh, chloride-containing environments where it exhibits superior properties. The critical pitting temperature (CPT), was determined in 6% $FeCl_3$ according to the ASTM G48A specification [14]. The critical crevice corrosion temperature, CCT, was determined using crevice formers of MRI-2 type, according to a modified ASTM G48 method. As demonstrated in Fig. 9, the 2707 steel despite the lower PREN in comparison to 3207HD (Table 6), has the highest CPT. Nevertheless, CCT levels of 2707 and 3207 are the same and higher than 2507. [16][17]

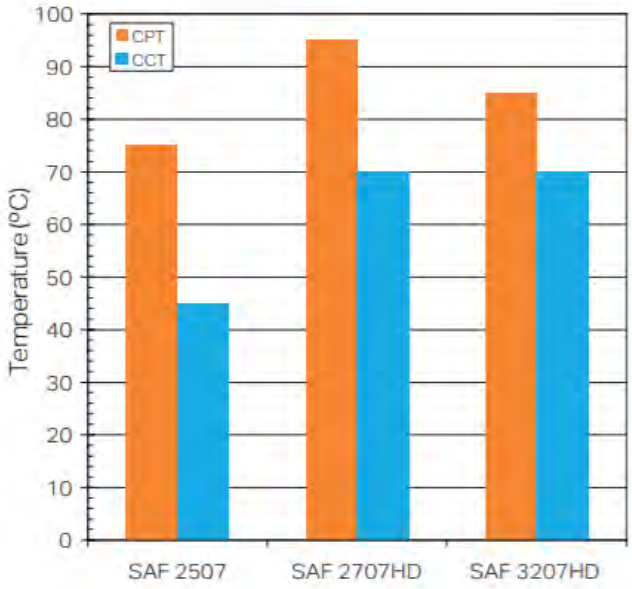


**Fig. 9**: CPT, CCT assessed using modified G-48A and MTI-2 testing.[16]

According to the literature, potentiostatic CPT measurements have been made under 750 mV/SCE anodic potential and showed that the CPT of 2707 was 64ºC in 3.5 wt.% NaCl solution. As depicted in Fig.10, pitting corrosion starts at 64ºC according to the criterion of 100 $\mu A/cm^2$. [19] The CPT in NaCl is lower than in $FeCl_3$ due to its aggressivity .

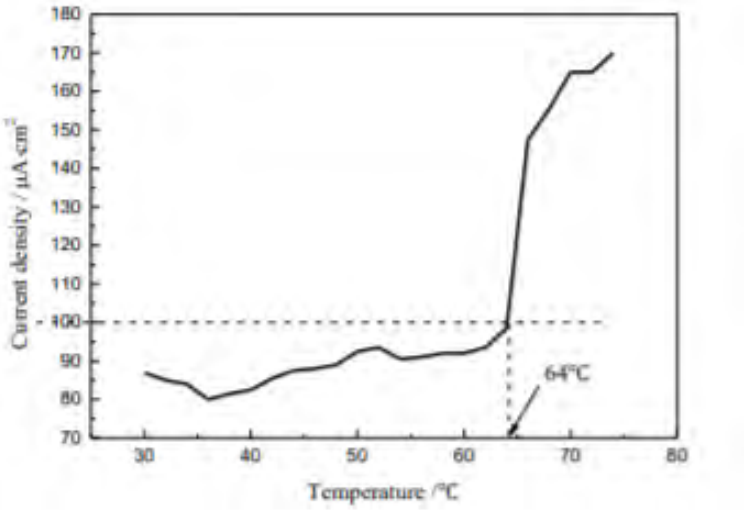


**Fig. 10:** Potentiostatic polarization results of 2707 at 750 mV/SCE in 3.5 wt.% NaCl solution. [19]

Furthermore, the SCC resistance of HDSS in chloride solutions at high temperatures is superior than the austenitic stainless steels (304, 316, Sanicro 28). (Fig. 11)

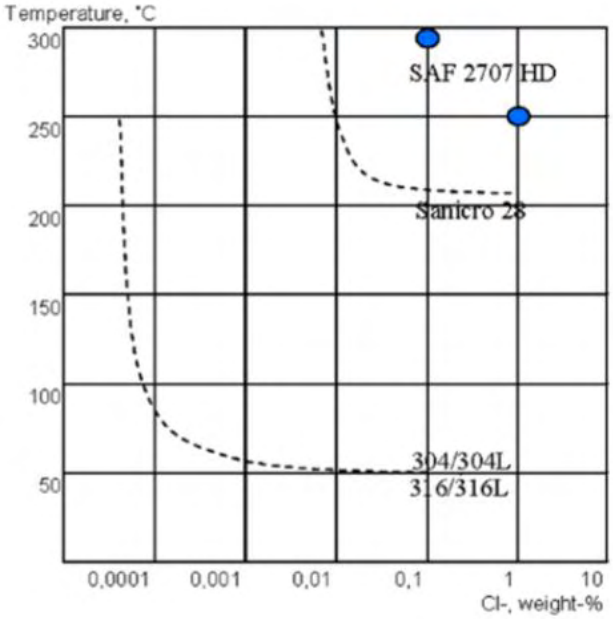


**Fig.11**: Comparison of stress corrosion cracking resistance of HDSS and austenitic stainless steels.[16]

In addition, the HDSS 2707, is considered as a highly corrosion resistance steel due to the well-maintained $Cr_2O_3$ surface film. Researchers showed that there are three corrosion potentials for chromium containing stainless steels in acidic chloride solutions.:

i) The electrochemical hydrogen evolution reaction (HER) from $H^+$ to $H_2$ on the bare chromium surface due to cathodic activation and the active anodic dissolution of chromium give the first stable corrosion potential ($E_{corr-1}$).

ii) After that, in the active-passive zone it appears the second unstable corrosion potential ($E_{corr-2}$).

iii) And finally, when the hydrogen evolution reaction on the oxidized chromium surface coupled with the anodic dissolution of passivated chromium give the third stable corrosion potential ($E_{corr-3}$). Surface and environmental conditions determine if the unstable corrosion state ($E_{corr-2}$) will transfer into the stable anodic dissolution ($E_{corr-1}$) or to passivation state ($E_{corr-3}$).

The reaction of the hydrogen evolution during anodic dissolution of chromium may be:

$$Cr + H_2O + H^+ \rightarrow Cr^{2+} + H_2 + OH^- \qquad (2.2)$$

Furthermore, the addition of N to stainless steel improves both the strength and the resistance to pitting and crevice corrosion in $Cl^+$ containing solutions. N presence in the passive film/alloy surface stabilizes the film and prevents attack by $Cl^-$, while produced nitrate ions improve the resistance to pitting corrosion. In parallel, N controls the increase of the electric current density for pit initiation. [18]

### 2.3.2 Mechanical properties

As known, HDSS generally show a higher strength comparing to single phase austenitic or ferritic stainless steels. The yield strength of austenitic and duplex stainless steels is shown in Fig. 12. SAF 2707 HD and SAF 3207 HD have the higher yield strength and AISI 316L has the lowest. [15][16] This can be explained by the high alloying elements of HDSS that give high strength in contrast with austenitic or ferritic stainless steels.

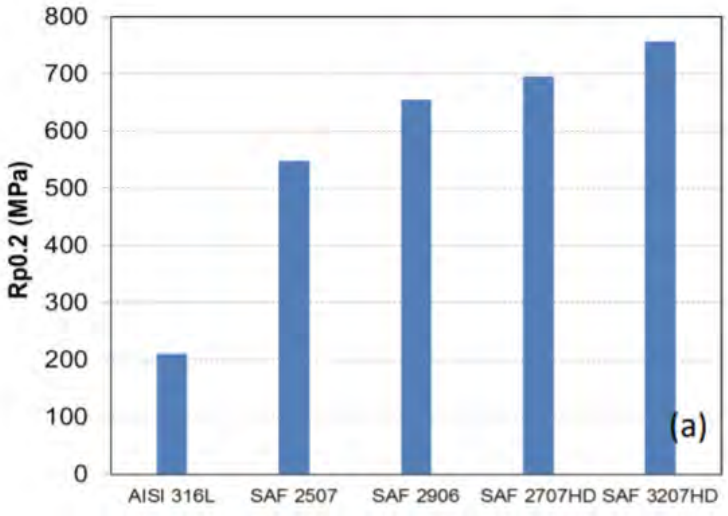


**Fig. 12:** Yield stress of austenitic and duplex stainless steels at RT.[15]

Figure 13 shows the influence of temperature on the Yield stress of the super and hyper duplex stainless steel tube materials with a wall thickness of up to 4 mm. SAF 3207 HD and SAF 2707HD have higher strength even at higher temperatures.

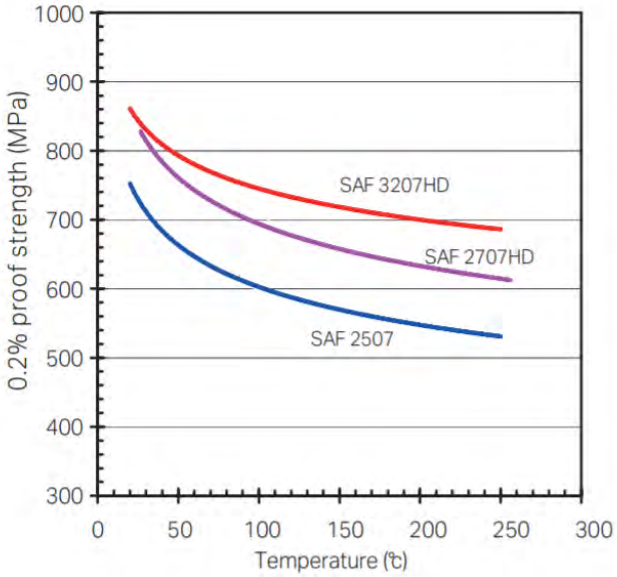


**Fig.13:** Influence of temperature on the super and hyper duplex stainless tube. [16]

Fig.14 shows the impact toughness of SAF 2707 HD and SAF 3207 HD at various temperatures. As shown, both grades have very high impact toughness. Although, SAF 2707 has a little higher impact toughness at temperatures above -100 $^{o}$C.

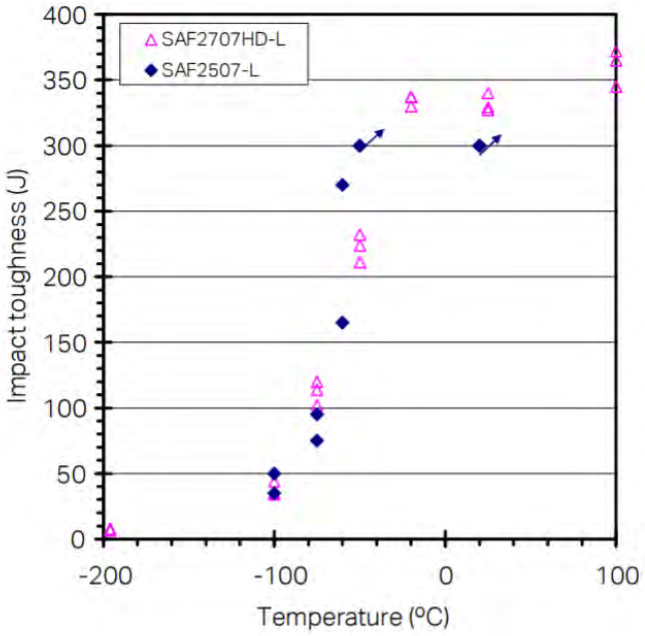


**Fig. 14**: Impact toughness of SAF 2507 and SAF2707 HD (Charpy-V 10x10mm) in the longitudinal directions. [16]

# Chapter 3: Experimental Procedures

## 3.1 Material

The material used for the experiments was the HDSS S32707. Table 8 shows the chemical composition of the material and its PREN.

**Table 8:** Chemical Composition (wt%) and PREN of S32707.

| Grade | UNS No | C | Cr | Ni | Mo | N | Mn | Co | Si | S | PREN |
|---|---|---|---|---|---|---|---|---|---|---|---|
| 2707 | S32707 | 0,03 | 27 | 6,5 | 4,8 | 0,4 | 1,5 | 1,0 | 0,5 | 0,01 | 48 |

The PREN, was calculated according to equation (2.1).

## 3.2 Preparation of specimens

Standard preparation included cutting, grinding and polishing in order to ensure proper shape and surface quality for the CPPT and CPT tests. The material was delivered as a tube with 2cm diameter, so it was necessary to be cut in longitudinal and transverse direction as depicted in Fig. 15. Cutting was performed with Struers ‘‘Accutom 2’’.

The outer surface of the specimens was grinded with SiC papers 120, 320, 500, 800, 1000 and 2000 grit and then polished with 3μm and 1μm diamond paste. Specimens were mounted in PTFE (Polytetrafluoroethylene) and sealant tape with the addition of a wire in order to be properly prepared for the corrosion tests (Fig.16). In order to determine the good connection between the specimen and the wire, a voltmeter was used. If the resistance between specimen and wire was close to zero, then the connection was acceptable. The exposed area was A=0.54-0.99 $cm^2$

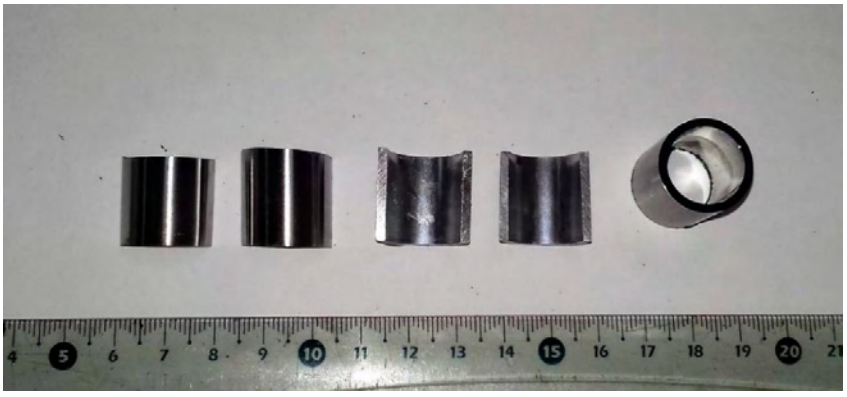

**Fig. 15**: Cut and polished specimens.

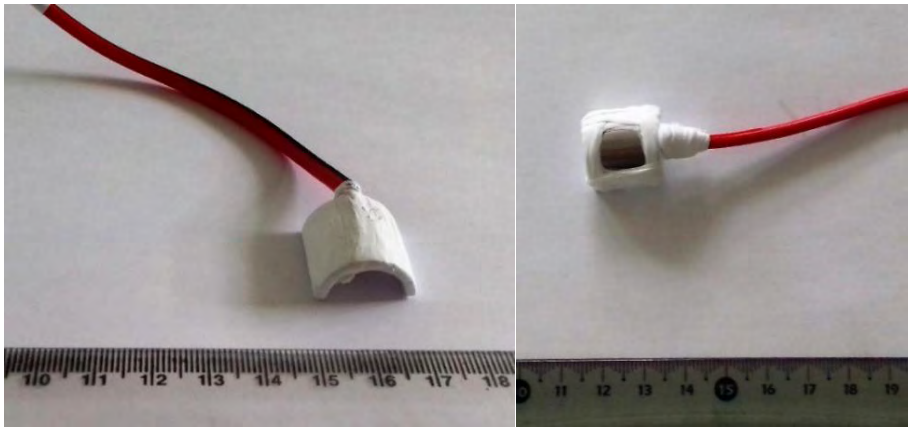

**Fig. 16**. Specimens before the CPP tests

## 3.3 Cyclic Potentiodynamic Polarization test (CPP)

Cyclic Potentiodynamic Polarization measurements were carried out in aerated 3,5 % wt. NaCl solution, at 25 $^{o}$C ambient temperature, which simulates seawater conditions. The device used for the electrochemical measurements is the galvanostat-potentiostat Gill AC 1044 from ACM Instruments in combination with the respective software (Figs.17,18). All the measurements were conducted according to ASTM G5-94 (2004), ASTM G61-86 (2014) and ASTM G71-81 (2014). [20][21][22]

The galvanostat adjusts the polarized current automatically in order to control the potential between the active electrode (WE) and the reference electrode (RE). This device changes the potential with a stable rate and records the current density penetrating the electrochemical cell.

Platinum electrode was used as the counter electrode (AE), silver chloride electrode (Ag/AgCl) as the reference electrode (RE) and the specimen as the working electrode (WE). This type of electrode is very common in corrosion tests according to ASTM G5-94 and G61-86. [20][21]

The electrolyte was prepared with distilled water in order not to influence solution's conductivity while buffer solution was used in order to keep the pH at 7.

The parameters fixed for the CPP tests were the following:

- Open circuit equilibrium time: 1 hour
- Potential range: -1500 mV up to +1500 mV as to open circuit/equilibrium potential ($E_{rest}$).
- Scan rate: 10 mV/min.

The polarization test starts with 1-hour equilibrium stage. During this stage, the specimen remains into the solution without current enforcement by the galvanostat-potentiostat. The

device records the potential and the current density that characterize the specimen into the specific electrolyte. The aim of this stage is to reach equilibrium on the surface of the specimen.

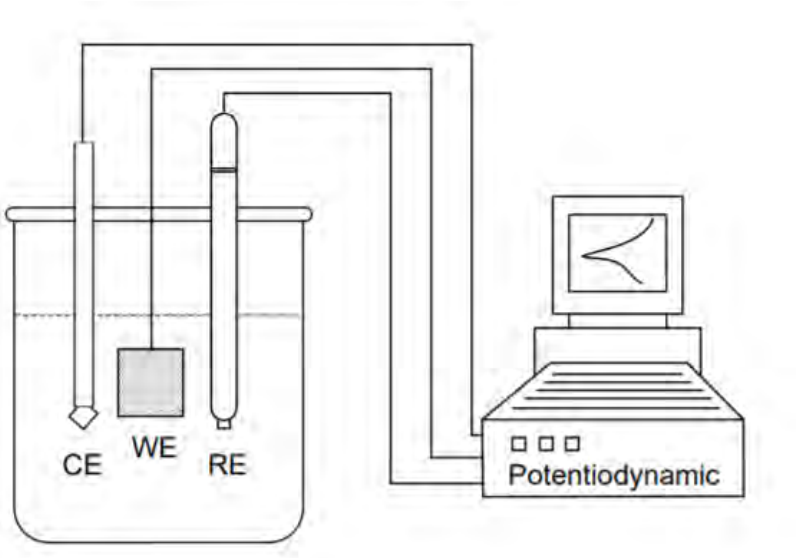


**Fig.17**. A typical set up for potentiodynamic measurements.[14]

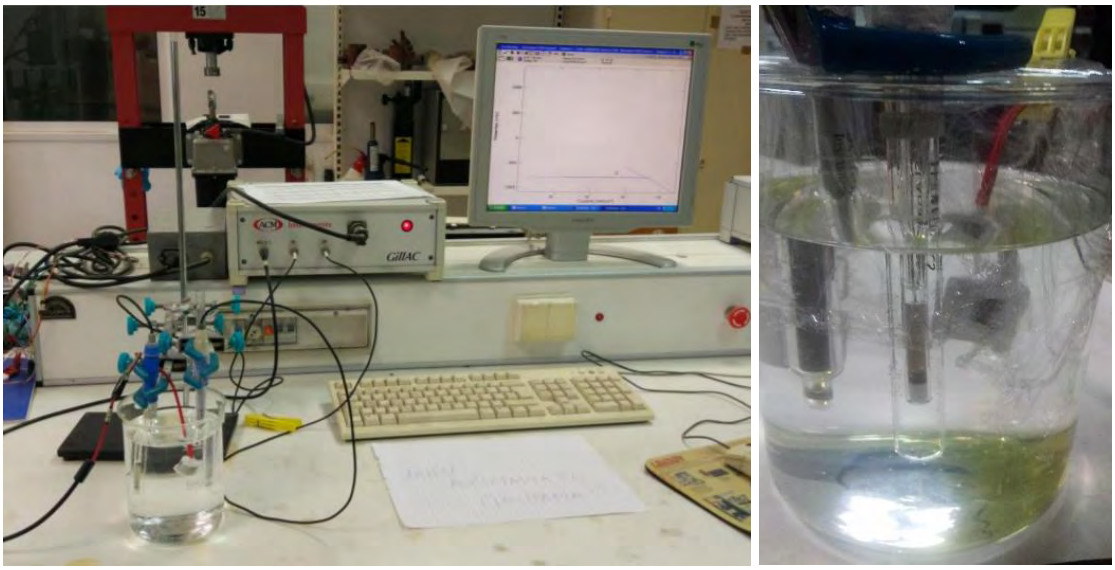

**Fig. 18**. Experimental set up.

## 3.4 Critical Pitting Temperature (CPT) Test

A potentiostatic technique was used to determine the Critical Pitting Temperature (CPT). This method is independent from the potential and the measurements were carried about in aerated 5% wt. NaCl solution. The anodic potential was 700-800 mV and the temperature increased at 1 $^{o}$C/min. The CPT is considered the temperature at which the current increases above 0.1 mA/cm$^2$ and remains above this critical current density for a minimum of 60 sec. CPT setup

was the same as the CPPT, with the exception that a heater (ARE Heating Magnetic Stirrer VELP SCIENTIFICA), a thermometer and a thermocouple were added to control and scan the temperature. All the measurements were conducted according to ASTM G150-99(2004) and the selection of the electrodes was according the information provided above for the CPP test.[26]

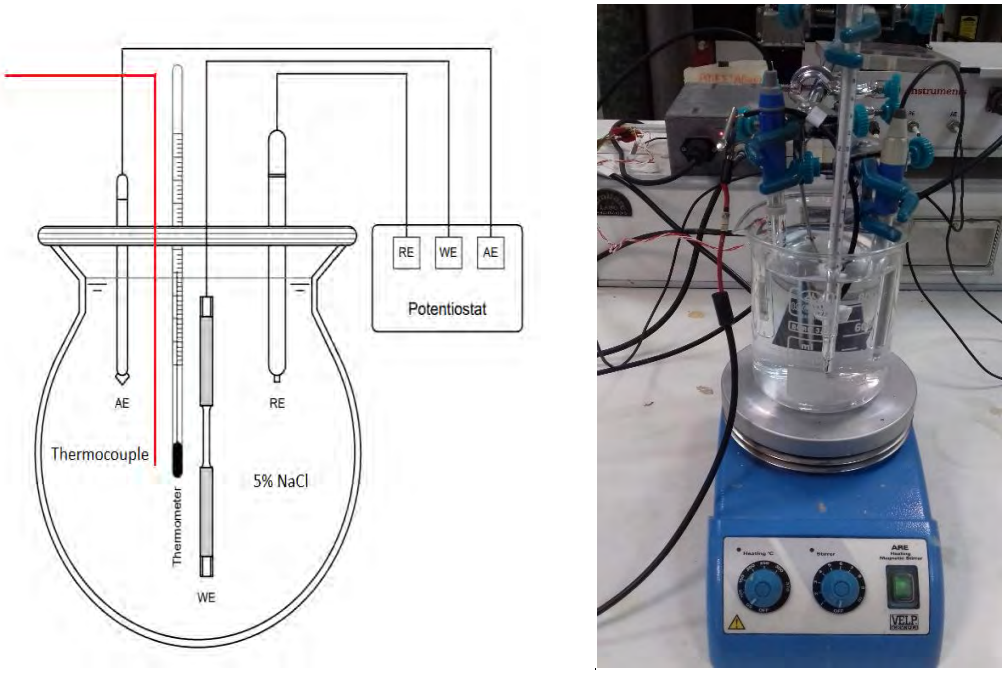


**Fig. 19**. CPT setup.

## 3.5 Processing the results of CPP test

Upon the completion of the CPPT the software gives a list of the recorded potentials and the respective current densities. The construction of the polarization curves requires plotting of potential values versus absolute values of current density. Having constructing these plots, useful conclusions can be drawn by the Tafel extrapolation and the calculation of the corrosion rate. For the characterization of the corroded surface of the specimens, full metallographic analysis was then conducted.

## 3.6 Processing of the results of CPT test

After the completion of the Critical Pitting Temperature test, the software provides a list of the recorded current densities and the relevant temperatures. The critical temperature is defined when the current density exceeds the criterion of 0.1 $\mu A/cm^2$ according to ASTM G150-99(2004). [26]

## 3.7 Stereoscopy

The corroded surfaces were initially examined under a stereoscope in order to define the severity of pitting corrosion on a macroscale level. A Leica ‘‘Wild M3Z’’ stereo-optical microscope was used at magnifications 6.5x – 40x.

## 3.8 Optical microscopy

The corroded surfaces and respective transverse cross-sections were examined in an optical metallographic microscope in order to acquire further information about the mechanism of corrosion. For this purpose, Leitz “Aristomet” was used, at magnifications 50x-500x. The metallographic preparation steps included specimen’s mounting in resin, grinding with SiC papers 120, 320, 500, 800, 1000 and 2000 grit, polishing with 3μm diamond paste and then electrolytic etching in 10% oxalic acid (10V, 15 sec and 7 flowrate) according to ASTM A262 [23]

## 3.9 SEM/EDX Analysis

The specimens were further examined by energy-dispersive X-ray spectroscopy (EDX). Line scans and local chemical analysis contributed to the identification of the corrosion mechanism. A SEM JEOL- 840A combined with EDS analysis was employed.

## 3.10 Atomic absorption spectrometry (AAS) Analysis

The solution collected at the end of each polarization test was further analyzed by Atomic absorption spectrometry (AAS) method in a Perkin Elmer 3300 device. The most important stage of atomic absorption is when the sample is vaporized. When the solution sample, in the form of small drops, reaches high temperature, it evaporates leaving salt particles and then part of them is broken down into free atoms. Therefore, high thermal energy is required. The Atomic Absorption method is based on the number of atoms formed in the flame space. [24]

## 3.11 XPS Analysis

Experimental XPS analyses were performed on a Kratos Analytical AXIS UltraDLD system, with Aluminum Monochromatic X-Ray source (λKa= 1.4866 Å), under high vacuum conditions ($10^{-8}$ torr). The spectra in all of the cases were calibrated by the standard method and were fixed according to the C *1s* peak at 284.6 ±0.2 eV of binding energy (B.E.). Wide-scan spectra (full range) were recorded by 160 eV of passing energy during a 2sweep scan, while High-Resolution (HR) regions by pass energy 20 eV during a three-sweep scan for C 1s and O 1s orbitals and by pass energy 80 and 4 sweep scan for the rest elements. Shirley and linear baseline was used to subtract the background per case, from the HR peaks and the experimental curves were fitted by a combination of Gaussian (70%) and Lorentzian (30%) distributions.

# Chapter 4: Results & Discussion

## 4.1 Cyclic Potentiodynamic Polarization curves

CPP tests were conducted both on hollow and convex surfaces of the specimens (inner and outer surface of the tube respectively). In Figs 20, 21 and 22 below representative polarization curves as extracted from the CPPT are given. In Fig. 20 the results regarding the convex surfaces are provided, while Fig. 21 contains the relevant results of the hollow surfaces. All curves are shown in Fig. 22 for comparison. A comparison to the results presented in [1] - which referred to 2 hours' open circuit equilibrium time- are given in Chapter 5 hereinafter.

Tables 9 and 10 sum up the results of CPP of S32707 in 3,5 %wt. NaCl solution. Potential range: -1500 mV - +1500 mV as far as the open circuit potential $E_{rest}$.

**Table 9**: Electrochemical values of HDSS 2707 immersed in 3,5% wt. NaCl, at 25 ºC.

| test | $E_{corr}$(mVvs. Ag/AgCl) (mV) | $E_{a/ctr}$(mVvs. Ag/AgCl) (mV) | $E_b$ (mVvs. Ag/AgCl) (mV) | $E_{cp}$ (mVvs. Ag/AgCl) (mV) | $E_{a/ctr}$-$E_{corr}$ (mV) | $E_{cp}$-$E_{corr}$ (mV) | $E_b$-$E_{cp}$ (mV) | $E_b$-$E_{corr}$ (mV) |
|---|---|---|---|---|---|---|---|---|
| 13 | -132,83 | 592,09 | 925,48 | -79,505 | 724,92 | 53,325 | 1004,985 | 1058,31 |
| 14 | -123,44 | 699,62 | 959,15 | -68,047 | 823,06 | 55,393 | 1027,197 | 1082,59 |
| 6 | -128,89 | 198,06 | 976,78 | -83,027 | 326,95 | 45,863 | 1059,807 | 1105,67 |
| 17 | -114,73 | 673,87 | 989,28 | -49,302 | 788,6 | 65,428 | 1038,582 | 1104,01 |

$E_{corr}$: corrosion potential; $E_{a/c\ tr}$: anodic-to-cathodic transition potential; $E_{cp}$: critical "passivation" potential; $E_b$: breakdown potential.

**Table 10:** Data extracted from Tafel extrapolation on the polarization curves of HDSS 2707:

| Test | $i_{corr}$ (mA/cm²) | $B_c$ (mV/decade) | $A_c$ (mV) | $Rc^2$ | ΔE(mVvs. Ag/AgCl) | Δi (mA/cm²) | $i_p$ (mA/cm²) |
|---|---|---|---|---|---|---|---|
| 13 | 0,00000389 | -308,31 | -32,435 | 0,999 | (-216,52)-(-182,68) | (0,001401)-(0,0001403) | 0,0011922 |
| 14 | 0,0000239 | 1697,3 | 394,03 | 0,09801 | (-73,32)-(340,96) | (0,000401)-(0,0000403) | 0,0011339 |
| 6 | 0,0000859 | -404,79 | -67,859 | 0,9857 | (-242,26)-(-178,87) | (0,005124)-(0,0005142) | 0,0084563 |
| 17 | 0,0000347 | -305,44 | -42,765 | 0,999 | (-165,62)-(-164,55) | (-0,00054)-(0,00051) | 0,0012984 |

$i_{corr}$: corrosion current density; $B_c$: Tafel slope; $A_e$: constant in Tafel equation; $Rc^2$: regression coefficient of the linear fit; ΔE: overpotential range for the linear fit; Δi: current density ranges for the linear fit; $i_p$: current density in the middle of current limiting stage.

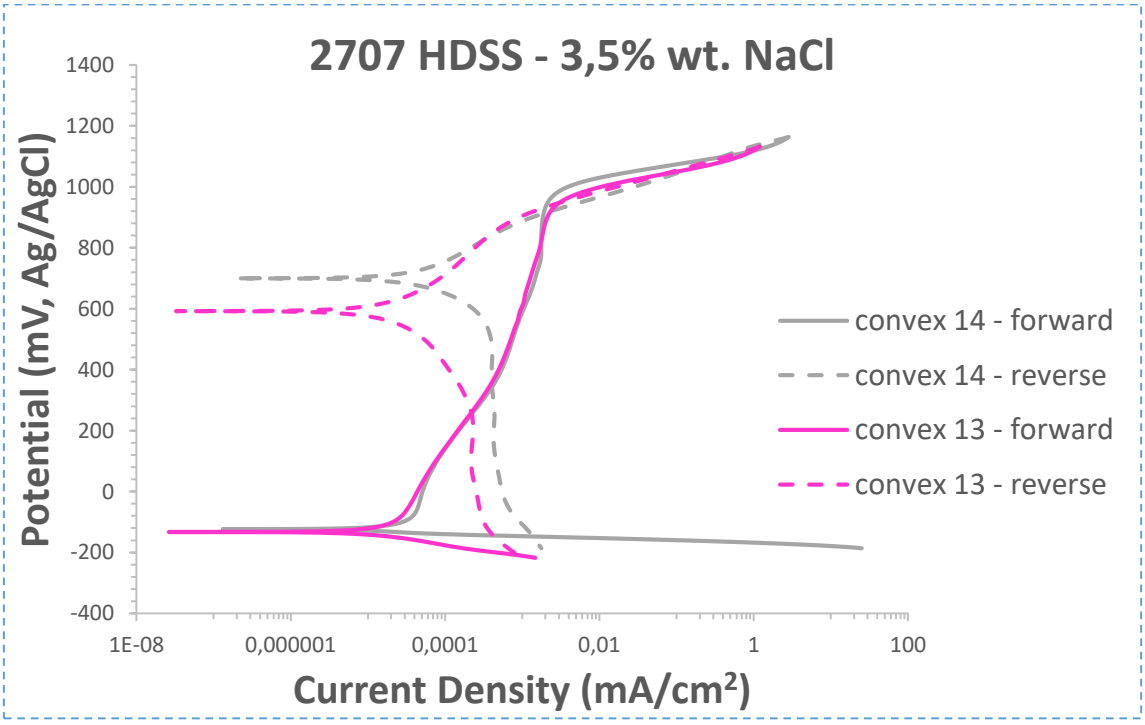


**Fig. 20:** Potentiodynamic polarization behavior of outer surface of the specimen.

The CPP curves were further analyzed and the results per test are presented analytically in the following paragraphs:

**Test 13:**

Test 13 corresponds to the examination of the curved surface of the specimen. At the anodic polarization, an active stage can be distinguished. This stage begins from the **corrosion potential $E_{corr}$=-132,83 mV**, where the current density increases sharply and the potential slightly. At this stage, oxidation/corrosion of the metal takes place. At the critical passivation potential $E_{cp}$, the current density changes with slow rate, tying to be stabilized, while potential values rise abruptly. In more detail, this stage is defined by the critical passivation potential (**$E_{cp}$=-89,505 mV**) and the **breakdown potential/pitting potential $E_b$=$E_{pitt}$=925,48 mV**. The range of this stage is **$\Delta E= E_b-E_{cp}$=1014,985 mV** and is considered as a real passivation stage because $i_p$<0,1 mA/cm$^2$. At the real passivation stage, a stable film of corrosion products is formed, which protects the surface from the solution. After the breakdown potential $E_b$ both current density and potential increase abruptly, oxidative processes can happen through the film and will likely lead to the destruction of the protective layer. Although, the breakdown potential occurs more than 1000mV higher than $E_{cp}$ and the likelihood of pitting corrosion is not high.

At this stage a negative hysteresis loop is noticed, but its area, which is set between the forward and the reverse potentiodynamic polarization curve, is too small. This is characteristic of an alloy that is highly resistant to localized corrosion. In addition, the difference between the $E_{pitt}$ and $E_{rep}$ and the area of the hysteresis loop shows the probability of pitting corrosion. At this test, the $E_{pitt}$ equals $E_{rep}$ and the hysteresis loop are very small, therefore there is a probability of high pitting corrosion resistance. T**he corrosion reverse potential, $E_{a/c\ tr}$= 592,09 mV**, is nobler than $E_{corr}$ and thus, the products of the corrosion at the reverse scan is nobler than the products formed at the forward scan.

To sum up, the hyper-duplex stainless steel S32707 at this test's conditions has high pitting corrosion resistance in 3,5% w.t. NaCl solution at a potential range of $E_b$= 925,48 mV to $E_{corr}$= -132,83 mV. Although, for potential values greater than $E_{rep}$ the severe attack of Cl ions destroys the protective film which indicate a limitation of 925,48 mV vs Ag/AgCl for applications of this HDSS.

**Test 14:**

Identical behavior was noticed in test 14, which was conducted as a repeat. In this case, a negative very small hysteresis loop appears as at test 13.

Breakdown potential is almost of the same size, **$E_b$=$E_{pitt}$= 959,15 mV**. Although, the corrosion reverse potential **$E_{a/c\ tr}$= 699,62** mV at this test is nobler compared to **$E_{corr}$= -123,44 mV** and the critical passivation potential is **$E_{cp}$=-68,047 mV**. The reverse polarization curve intersects the forward one at a potential value near **$E_b$**.

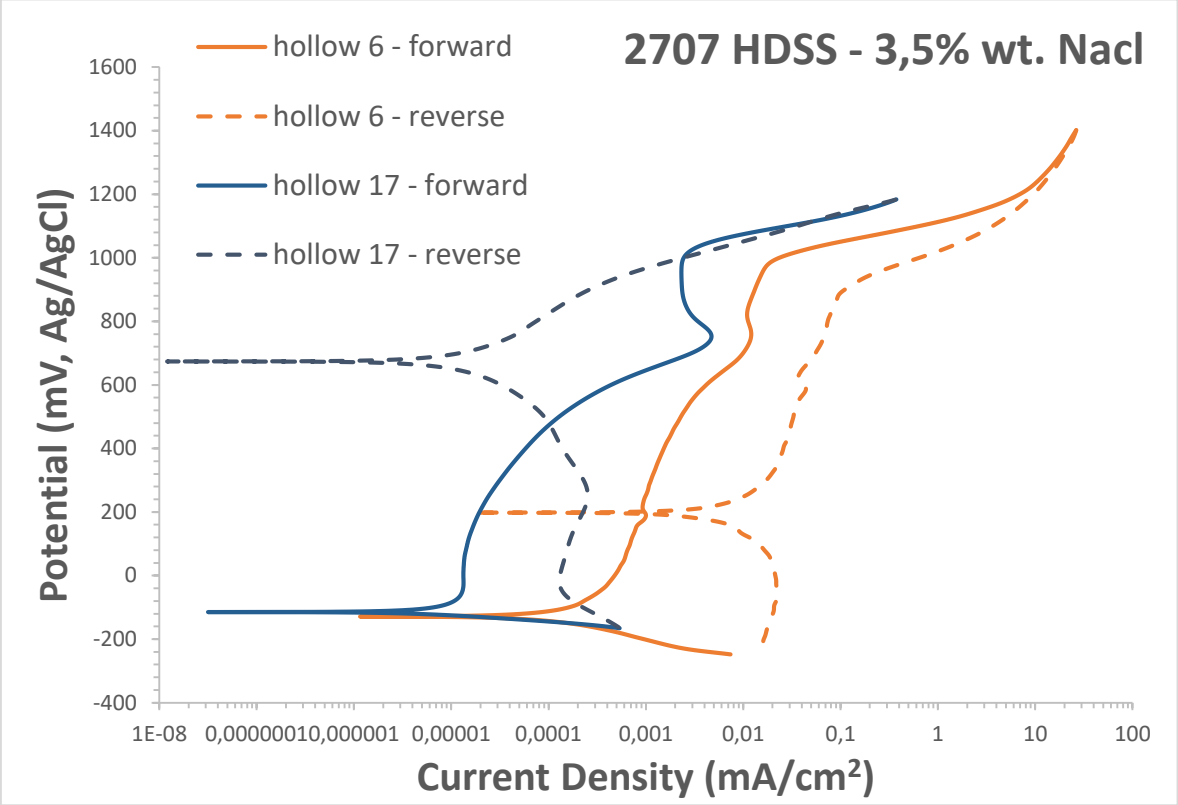


**Fig. 21**: Potentiodynamic polarization behavior of the inner surface of the specimen.

**Test 6:**

This specimen corresponds to the exposure of the inner surface of the tube (hollow surface).

At the anodic scan, five stages can be distinguished:

- **Stage 1:** The active stage begins from the **corrosion potential $E_{corr}$=-128,89 mV,** where the current density increases sharply and the potential slightly. At this stage, corrosion of the metal takes place initiating at surface defects.
- **Stage 2:** At the **critical passivation potential $E_{cp1}$=-49,167 mV**, the current density changes with slow rate, while the potential is increasing. This stage is limited by a slightly increasing of current density and it is called passivation stage.
- **Stage 3:** This stage starts from a **breakdown potential $E_{b1}$=607,51mV** to a **critical passivation potential $E_{cp2}$=756,68 mV**, at this stage both the potential and the current density increases slightly due to the formation of metastable pits.
- **Stage 4:** This stage begins at the potential $E_{cp2}$ **until the breakdown potential $E_{b2}=E_{pitt}$=980,54 mV** where the rate of the current density is being reduced, while the potential is increasing. Stage 4 can be characterized as **a real passivation stage** as $i_p \approx 0.01$ mA/cm$^2$. The range of the real passive stage is **$\Delta E=E_{b2}-E_{cp2}$=223,86 mV**. Passive regions are typically associated with the formation of relatively stable corrosion products on the surface of the sample, which prevents the penetration of the electrolyte.

- **Stage 5:** An abrupt increase in current density is noticed and the protective film is dissolved.

Furthermore, there is a negative hysteresis loop, which indicates the dissolution of the protective passive layer and pitting development. The pits begin to close during the repassivation stage at **the repassivation potential $E_{rep}$=193,66 mV**. The potential $E_{rep}$ is nobler than the $E_{corr}$ and the propagation of active pits is diminished or stopped. The $E_{rep}$ sets an upper limit (193,66 mV) for the application of S32707 in a chloride containing environment. At this test, the $E_{pitt}$-$E_{rep}$=786,88 mV and the hysteresis loop is not so small as before, therefore there is a probability of low pitting corrosion resistance.

Finally, **the corrosion reverse potential, $E_{a/c\ tr}$=198,06 mV** is nobler than $E_{corr}$ and thus the products of the corrosion at the reverse polarization is nobler than the products at the forward polarization.

**<u>Test 17</u>:**

Test 17 is a repeat of Test 6. It is obvious from Fig. 21 that the anodic scan is similar to the anodic scan of test 6.

In detail:

- **Stage 1** begins from **the corrosion potential $E_{corr}$=-114,73 mV** until **the critical passivation potential $E_{cp1}$=38,753 mV** where **stage 2** starts.
- **Stage 2** has a range of **$E_{b1}$-$E_{cp1}$=43,99 mV.**
- **Stage 3** extends from **a breakdown potential $E_{b1}$=87,75 mV** to a **critical passivation potential $E_{cp2}$=740,48 mV** where metastable pits are formed.
- **Stage 4**, known as **passivation stage** begin from the potential $E_{cp2}$ until **the breakdown potential $E_{b2}$=987,7 mV.**
- **Stage 5** continues with an abrupt increasing current density

At test 17, the cathodic scan differentiates from the cathodic scan of test 6. The hysteresis loop is very small which is a characteristic of a highly resistant to localized corrosion alloy.

Consequently, taking into account that the $E_{pitt}$ equals to $E_{rep}$, as well as the negligible hysteresis loop proves the high pitting corrosion resistance of the steel.

Finally, **the corrosion reverse potential, $E_{a/c\ tr}$=673,87 mV** is nobler than $E_{corr}$, which implies nobler surfaces.

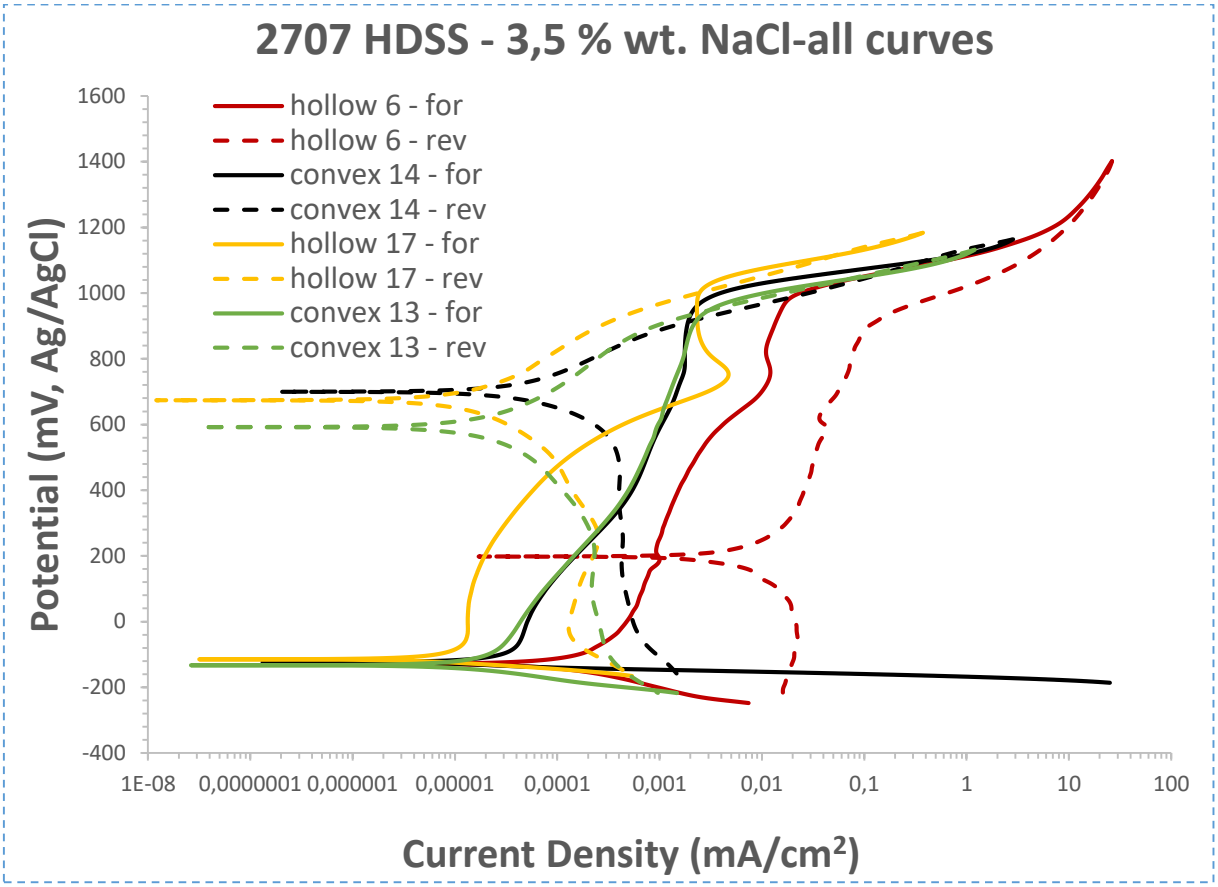


**Fig, 22**: Comparison of potentiodynamic polarization behavior between the outer and the inner surface of the specimen.

Fig. 22 provides a basis for the comparison of all the polarization curves. The conclusions drawn are summarized below:

- Corrosion potential $E_{corr}$ remains identical in every polarization test.
- Anodic-to-cathodic transition potentials ($E_{a/c\ tr}$) are always nobler than the corrosion potential $E_{corr}$. Thus all the products in the reverse scan are nobler than the forward.
- Convex surface specimens show similar behavior, while the hollow surfaces exhibit different behavior. More specifically, test 6 curve is placed to the right of the chart with $i_p$ close to 0,01 mA/cm$^2$. Surfaces with $i_p \approx$ 0,01 mA/cm$^2$ are characterized by a real passivation stage which associates with stable corrosion products on the specimen surface that prevent the electrolyte to penetrate. Bur when $i_p$ exceeds the 0,01 mA/cm$^2$, surfaces are characterized by pseudo-passivation stage.
- Negative hysteresis loop was not observed at test 13,14,17 while a small one was found at test 6.

The susceptibility of the specimen to active dissolution is determined by the evaluation of the corrosion current density $i_{corr}$ and the corrosion potential $E_{corr}$, while the passivation ability of is defined by the passivation current density $i_p$ and the passivation potential $E_p$. Also, the stability of the formed passive films is indicated by the passivation current density and the range of the passivation area.

- The corrosion current densities follow the sequence:

$$i_{corr\ (t\_13)} = 0{,}00000389\ mA/cm^2 < i_{corr\ (t\_14)} = 0{,}0000239\ mA/cm^2 < i_{corr\ (t\_17)} = 0{,}0000347\ mA/cm^2 < i_{corr\ (t\_6)} = 0{,}0000859\ mA/cm^2.$$

- The passivation current densities are classified as such:

$$i_{p\ (t\_14)} = 0{,}0011339\ mA/cm^2 < i_{p\ (t\_13)} = 0{,}0011922\ mA/cm^2 < i_{p\ (t\_17)} = 0{,}0012984\ mA/cm^2 < i_{p\ (t\_6)} = 0{,}0084563\ mA/cm^2.$$

$i_p$ express the conductivity of the surface film. The lower conductivity of the surface film the higher local corrosion resistance of the specimen.

- The difference between $E_{cp}$ and $E_{corr}$, represents the ability for passivation. Starting with the greater passivation ability the sequence is the following:

$$(E_{cp} - E_{corr})_{(t\_6)} = 45{,}863\ mV < (E_{cp} - E_{corr})_{(t\_13)} = 53{,}325\ mV < (E_{cp} - E_{corr})_{(t\_14)} = 55{,}393\ mV < (E_{cp} - E_{corr})_{(t\_17)} = 65{,}428\ mV.$$

→Test 6> Test 13> Test 14 > Test 17.

- The comparison of the difference between the breakdown potential $E_b$ and the corrosion potential $E_{corr}$ is shown by the following sequence, starting from the specimen with the lower corrosion resistance:

$$(E_b\text{-}E_{corr})_{(t\_13)} = 1058{,}31\ mV < (E_b\text{-}E_{corr})_{(t\_14)} = 1082{,}59\ mV < (E_b\text{-}E_{corr})_{(t\_17)} = 1104{,}01\ mV < (E_b\text{-}E_{corr})_{(t\_6)} = 1105{,}67\ mV.$$

→Test 13> Test 14> Test 17 > Test 6.

- Regarding the range of the passive region the sequence is the following:

$(E_b - E_{cp})_{(t\_13)} = 1004{,}985$ mV < $(E_b - E_{cp})_{(t\_14)} = 1027{,}197$ mV < $(E_b - E_{cp})_{(t\_17)} = 1038{,}582$ mV < $(E_b - E_{cp})_{(t\_6)} = 1059{,}807$ mV.

### 4.1.1 Corrosion rate

The corrosion rate can be determined via the calculation of the corrosion current density. By employing equations presented in 1.5.2, corrosion rate can be calculated and the results are summarized in Table 11. The calculated corrosion rates are particularly low and indicate a significant corrosion resistance. From the literature, high corrosion resistance means corrosion rate lower than 0,075 mm/y. [1] Highly alloyed materials, such as Alloy 59 and S32205 exhibit CR ~ 0,056 mm/y and 0,0043 mm/y respectively. These CR were calculated by conducting corrosion measurements in the same corrosive environment as the current work. [25]

**Table 11:** Corrosion rate

| | **Corrosion rate** | |
|---|---|---|
| Test | mpy | mm/y |
| 13 | 0,0015 | 0,00004 |
| 14 | 0,0094 | 0,00002 |
| 6 | 0,0341 | 0,00086 |
| 17 | 0,0133 | 0,00035 |

## 4.2 Stereoscopy

The stereoscopic analysis of the tests provided useful information about the corrosion behavior of HDSS 2707. The information from the stereoscopic analysis coincides with the analysis of the polarization curves. Figs. 23, 24, 25 and 26 depict the surface view of the specimens 13,14,6 and 17 respectively. The density and the size of the pits were measured and are presented in Table 12.

The morphology of the pit considered as elliptical and the size was calculated as hemispherical and thus the size is considered as the volume of a hemisphere:

$$S = \frac{4}{3}\pi\rho^3 \qquad (4.1)$$

Where, S is the size and ρ the radius.

**Table 12:** Results of density, size of the pits and surfaces' conditions

| Test | Density (pits/ $cm^2$) | Size ($mm^3$) | Salt deposits |
|---|---|---|---|
| 13 | 4,17 | 0,000345 | Yes |
| 14 | 4,45 | 0,000809 | Yes |
| 6 | 16,67 | 0,000098 | Yes |
| 17 | 12,12 | 0,000435 | Yes, severe |

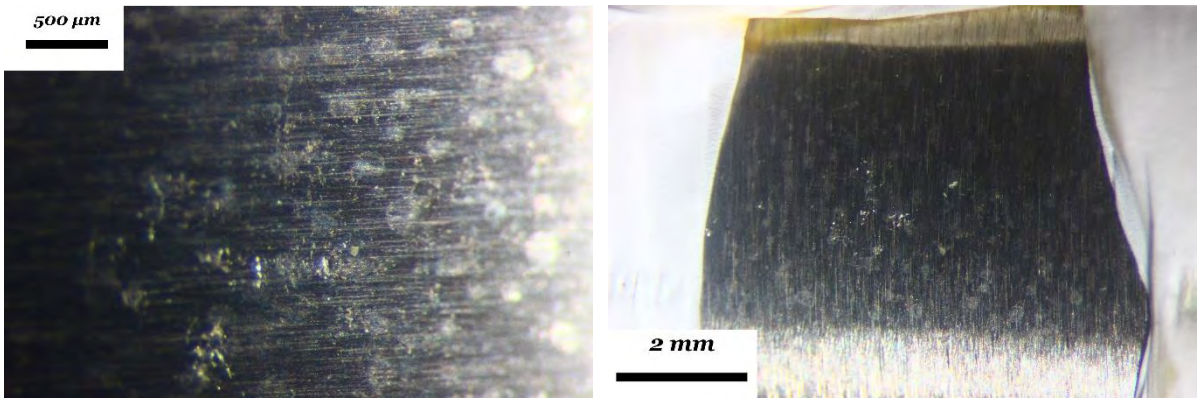


**Fig 23:** Surface view of specimen 13

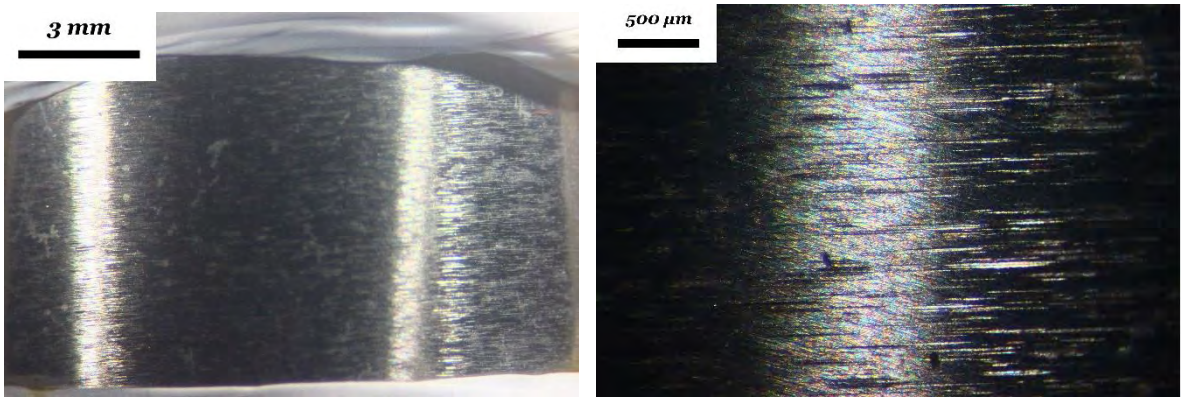


**Fig. 24:** Surface view of specimen 14

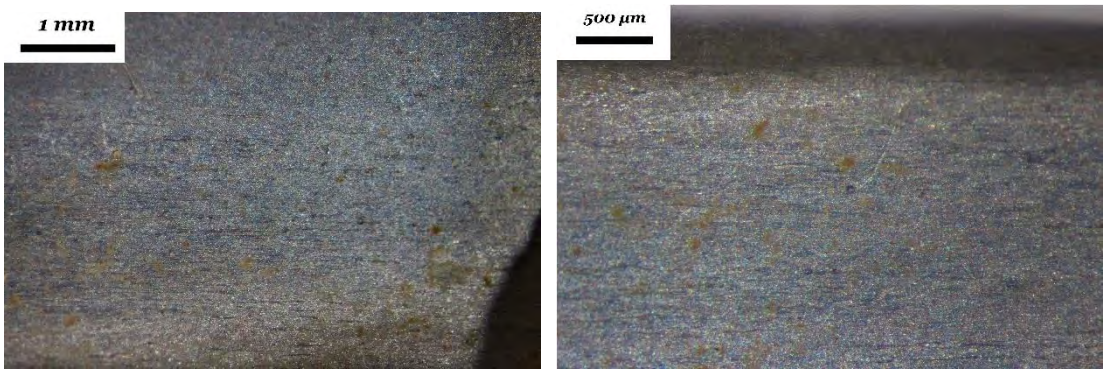


**Fig.25:** Surface view of specimen 16

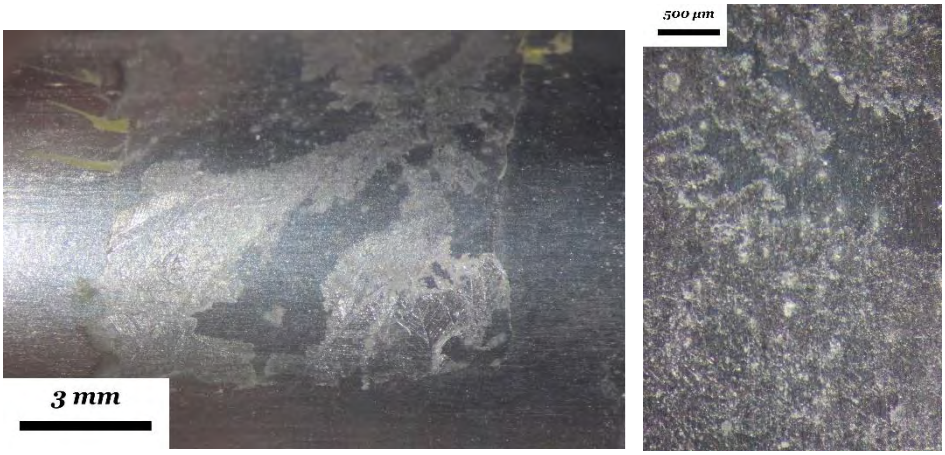


**Fig. 26:** Surface view of specimen 17.

The conclusions drawn from the optical examination are the following:

- Convex surfaces contained less pits than the hollow, this can be explained by the fact that pits initiate at preferred sites. The sites include the holder-specimen interface, metallic inclusions, the vapor-liquid interface in partially immersed specimens and imperfections in the passive films on the surface. It should be emphasized that convex surfaces were polished while hollows not.
- Convex surfaces had less severe deposits of salt.
- Regarding the density of pits (D), the sequence is the following:

$D_{t\_13} = 4{,}1667 \text{pits/cm}^2 < D_{t\_14} = 4{,}45 \text{ pits/cm}^2 < D_{t\_17} = 12{,}12 \text{ pits/cm}^2 < D_{t\_6} = 16{,}667 \text{ pits/cm}^2$.

- Regarding the size of pits S, the sequence is the following:

$S_{t\_6} = 0{,}000098 \text{ mm}^3 < S_{t\_13} = 0{,}000345 \text{ mm}^3 < S_{t\_17} = 0{,}000435 \text{ mm}^3 < S_{t\_14} = 0{,}000809 \text{ mm}^3$

## 4.3 Optical microscopy

A detailed microstructural examination was carried out in order to study the microstructure, the depth of the pits and to extract information on the corrosion mechanism.

Microstructure consists of ferrite and austenite, which correspond to the white and darker area respectively in Fig.27. In the specimen the white area starts to be consumed which means that the ferrite is more prone to pitting corrosion.

Furthermore, the depth of the pits as well as the morphology varies per specimen as shown in Table 13.

**Table 13.** Depth and shape of pits.

| Test | Depth (μm) | Shape |
|---|---|---|
| 6 | 14,756 (Fig. 17a) | elliptical |
| | 12,042 (Fig 27 b) | elliptical |
| 13 | 11,77 (Fig.28) | elliptical |
| 17 | 11,434 (Fig.29a,1) | narrow |
| | 10,973 (Fig.29,a,2) | narrow |
| | 6,955 (Fig.29,a,3) | narrow |
| | 14,536 (Fig. 29, a4 and Fig29,b) | narrow |
| | 11,035 (Fig. 29,c) | elliptical |

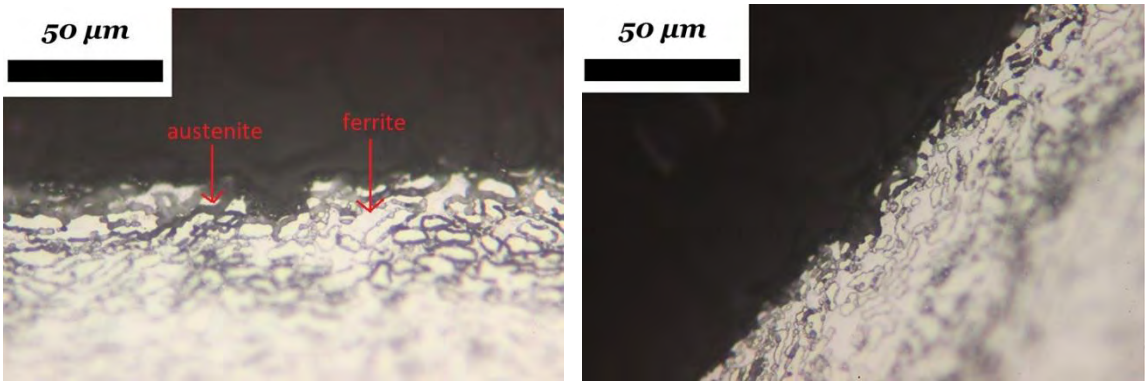


**(a)** **(b)**

**Fig.27:** Microstructure in specimen 6

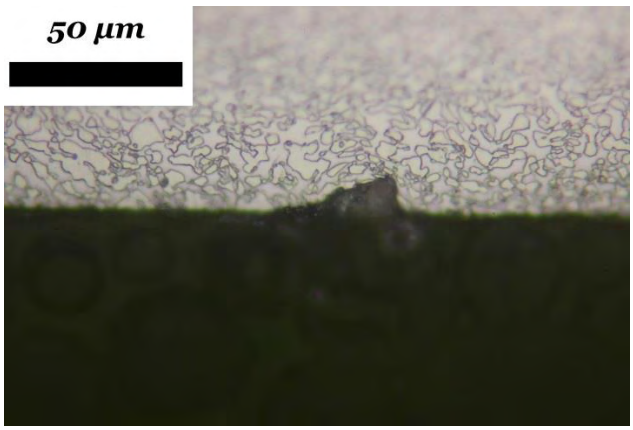


**Fig. 28**: Microstructure of the pit in specimen 13

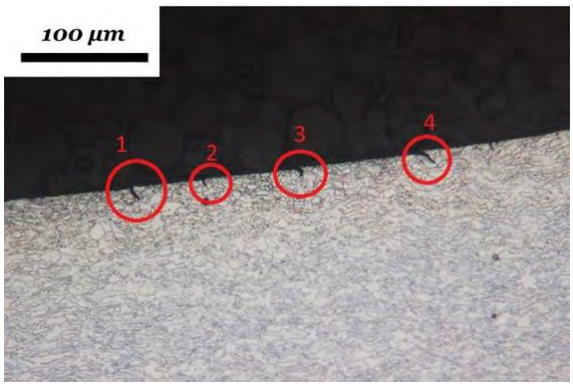


**(a)**

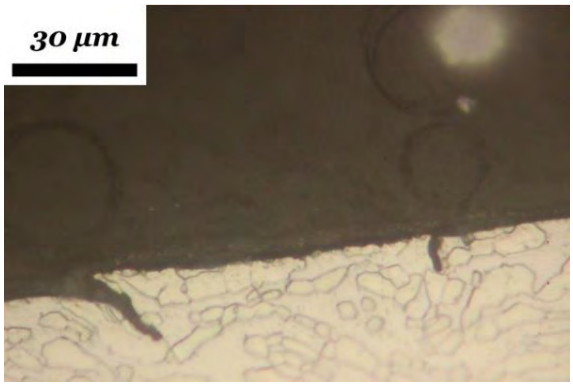


**(b)**

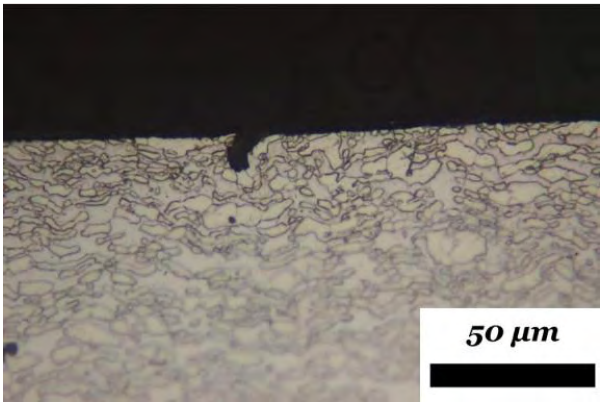


**(c)**

**Fig. 29:** Microstructure of the pits in specimen 17.

## 4.4 SEM/EDX Analysis

After the CPP test the specimens was examined by SEM/EDX on their surface and on the cross section as well.

### 4.4.1 Surface examination

In Figs.30-34, semi- quantitive local chemical analysis results are given. On the exposed surface several small pits alongside to “surface irregularities” from where pits initiate were observed. Figs. 31,32 shows significant Cl presence, which indicate that Cl ions had penetrated inside the pits.

The line scans conducted across the pits (Fig. 32,33,34) demonstrate that Fe and Cr concentrations were reduced inside the pits and the surface irregularities as well. The reduction of Cr indicates the dissolution of the protective passive film Cr-O due to the severe attack of the Cl ions.

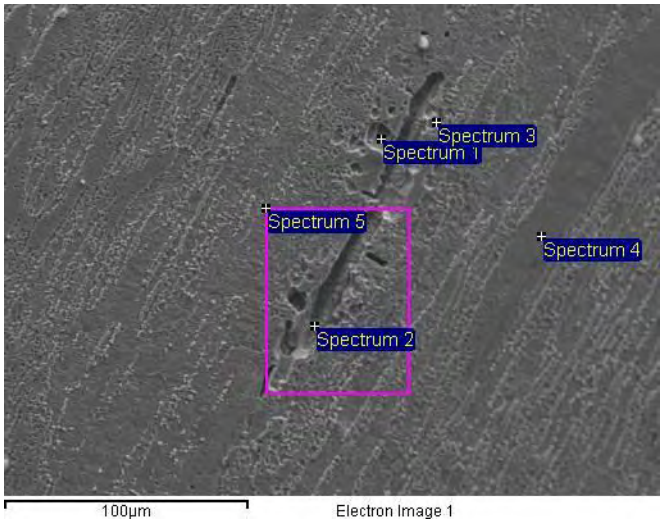


Processing option : All elements analysed (Normalised)

| Spectrum | In stats. | C | O | S | Cr | Mn | Fe | Ni |
|---|---|---|---|---|---|---|---|---|
| Spectrum 1 | Yes | 15.51 | 4.69 | 2.68 | 24.32 | 0.70 | 47.93 | 4.17 |
| Spectrum 2 | Yes | 20.76 | 9.83 | 1.93 | 20.77 | 1.24 | 41.02 | 4.45 |
| Spectrum 3 | Yes | 25.58 | 12.43 | 2.27 | 18.83 | 0.60 | 37.25 | 3.05 |
| Spectrum 4 | Yes | 25.34 | 9.85 | 1.75 | 19.54 | 0.43 | 39.24 | 3.85 |
| Spectrum 5 | Yes | 24.16 | 13.68 | 1.63 | 18.85 | 0.68 | 37.66 | 3.35 |

**Fig. 30**: Spot chemical analysis at the surface of the corroded specimen

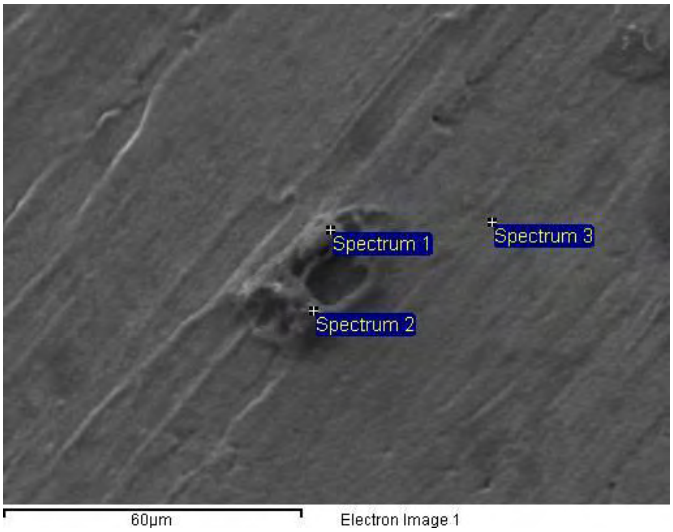


Processing option : All elements analysed (Normalised)

| Spectrum | In stats. | C | O | Na | Si | Cl | Cr | Fe | Ni | Mo | Total |
|---|---|---|---|---|---|---|---|---|---|---|---|
| Spectrum 1 | Yes | 52.82 | 26.49 | 8.65 | 0.57 | 3.49 | 1.31 | 3.60 | 0.32 | 2.75 | 100.00 |
| Spectrum 2 | Yes | 59.49 | 29.58 | 3.31 | 0.34 | 2.17 | 1.23 | 2.19 | 0.04 | 1.65 | 100.00 |
| Spectrum 3 | Yes | 13.36 | 2.07 | 0.01 | 0.98 | 0.51 | 24.34 | 51.65 | 1.98 | 5.11 | 100.00 |

**Fig. 31**: Spot chemical analysis at the surface of the corroded specimen

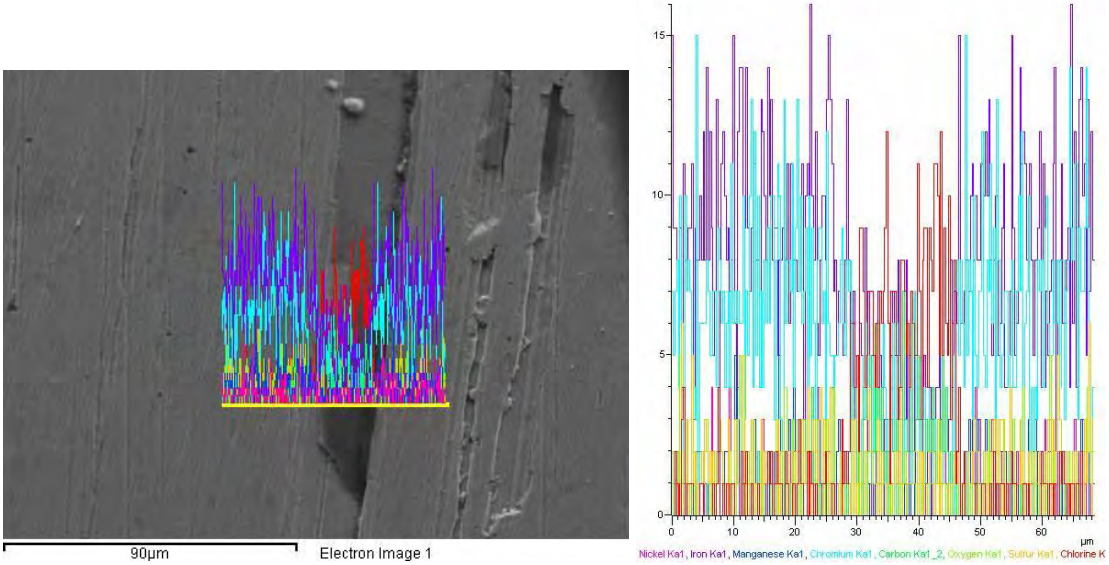


**Fig. 32**: Line scan on the specimen

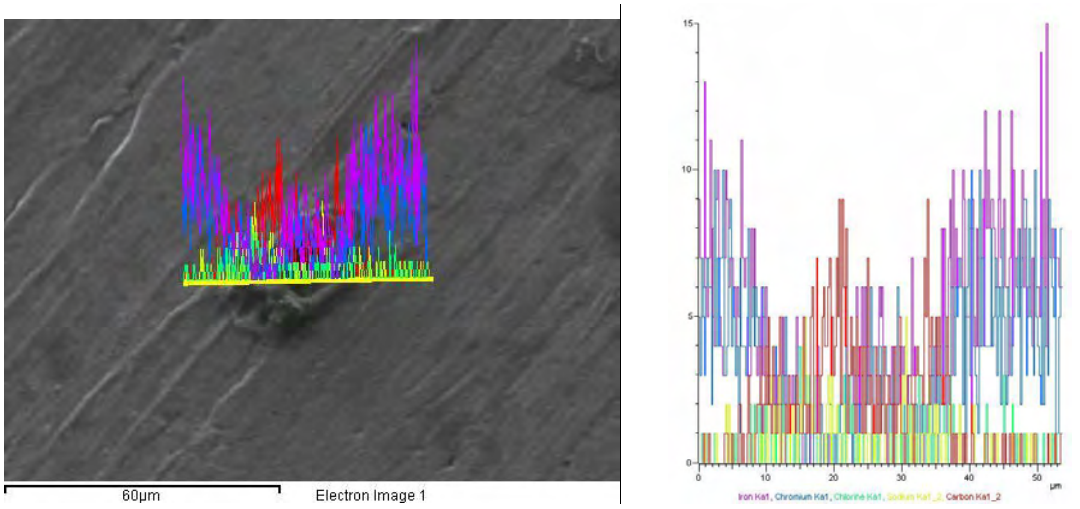


**Fig. 33**: Line scan on the specimen

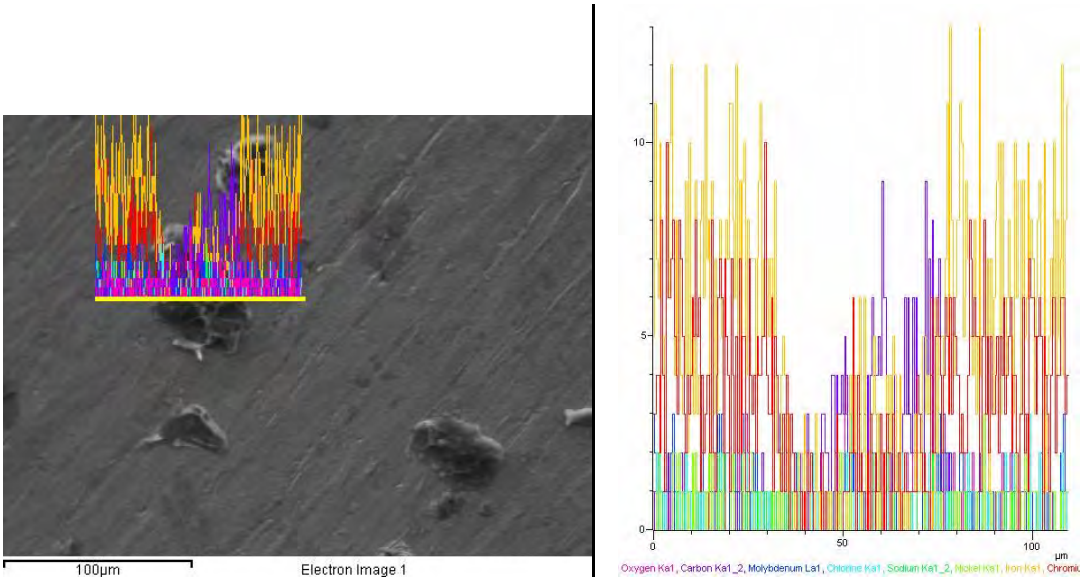


**Fig. 34**: Line scan on the specimen

## 4.4.2 Cross-section examination

Fig. 35 and 36 depict the results from the transverse cross-section of the corroded specimens.

Inside the pit area, a remarkable reduction of the concentration in Cr, Ni and Mo has been detected. Cl was detected the side surface of the pits.

The relevant line scans (Fig. 37,38,39) show that the protective passive film has been dissolved as proved by the absence of Cr on the side surfaces of the pits.

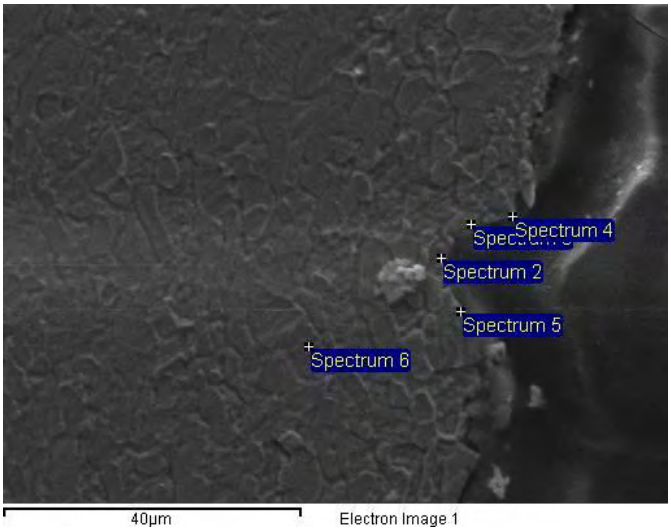


Processing option : All elements analysed (Normalised)

| Spectrum | In stats. | O | Si | Cl | Cr | Fe | Ni | Mo | Total |
|---|---|---|---|---|---|---|---|---|---|
| Sum Spectrum | Yes | | | | 28.71 | 59.35 | 5.46 | 6.48 | 100.00 |
| Spectrum 2 | Yes | 12.89 | 0.84 | 1.28 | 23.52 | 51.96 | 4.62 | 4.89 | 100.00 |
| Spectrum 3 | Yes | 8.94 | 0.69 | 0.12 | 24.79 | 53.70 | 7.03 | 4.74 | 100.00 |
| Spectrum 4 | Yes | 45.47 | | 4.58 | 18.28 | 26.97 | | 4.71 | 100.00 |
| Spectrum 5 | Yes | 30.39 | | 5.59 | 18.84 | 37.49 | | 7.70 | 100.00 |
| Spectrum 6 | Yes | 0.74 | | -0.44 | 29.61 | 56.98 | 7.45 | 5.66 | 100.00 |

**Fig. 35**: Spot chemical analysis closer to the pit in transverse cross-section.

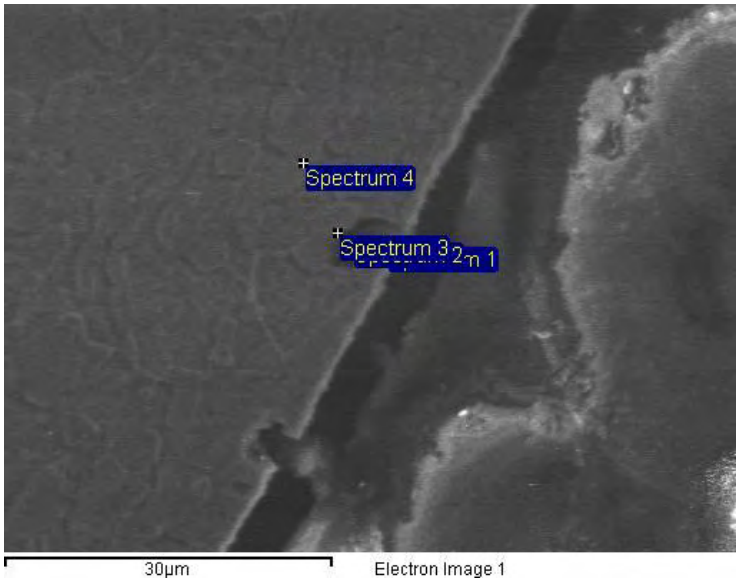


Processing option : All elements analysed (Normalised)

| Spectrum | In stats. | O | Si | Cl | Cr | Fe | Ni | Mo | Total |
|---|---|---|---|---|---|---|---|---|---|
| Spectrum 1 | Yes | 46.85 | 1.04 | 13.72 | 9.75 | 24.70 | 2.56 | 1.38 | 100.00 |
| Spectrum 2 | Yes | 32.22 | 0.26 | 10.03 | 11.82 | 38.99 | 6.68 | | 100.00 |
| Spectrum 3 | Yes | 23.31 | | 4.50 | 22.59 | 38.97 | 4.94 | 5.69 | 100.00 |
| Spectrum 4 | Yes | 0.24 | 0.33 | -0.01 | 27.97 | 61.93 | 6.09 | 3.45 | 100.00 |

**Fig. 36**: Spot chemical analysis closer to the pit in transverse cross-section.

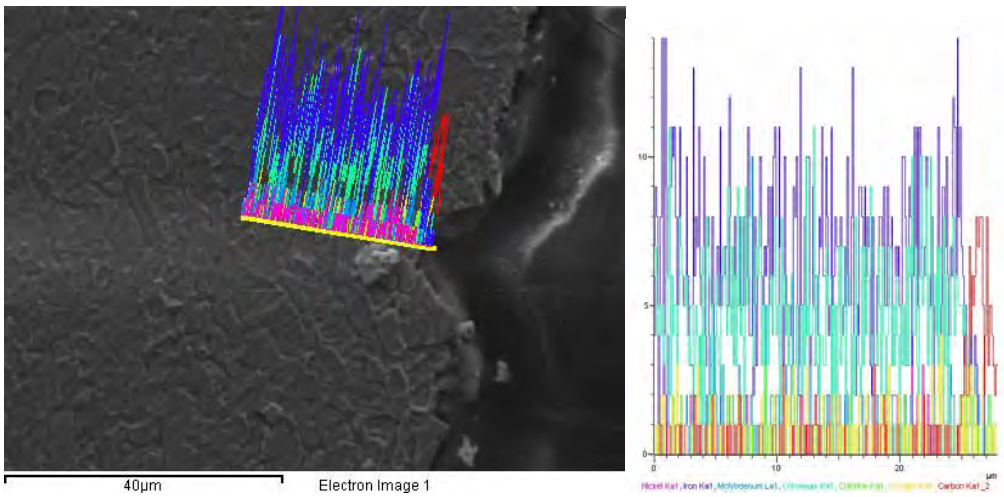


**Fig. 37**: Line scan at the edge of the pit.

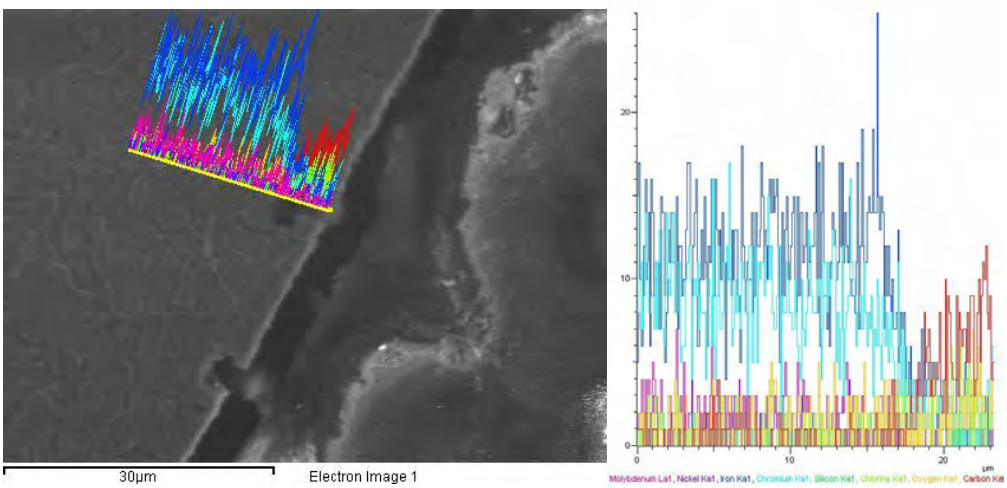


**Fig. 38** : Line scan at the edge of the pit.

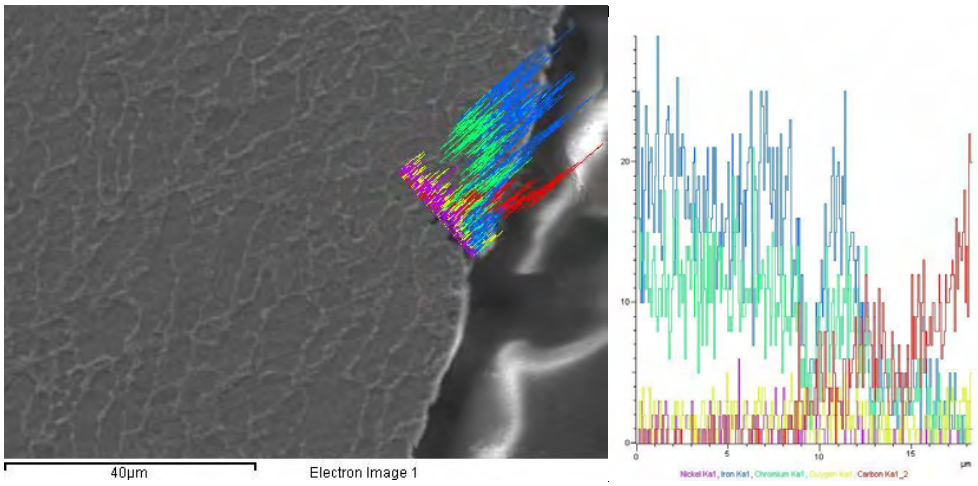


**Fig. 39** : Line scan at the edge of the pit.

## 4.5 Atomic absorption spectrometry (AAS) Analysis

AAS analysis was conducted in the NaCl solution collected after the CCPT. The results of the AA analysis are presented in Table 14.

**Table 14:** Results of AAS Analysis.

| Specimen | Cr (ppm) | Ni (ppm) | Fe(ppm) |
|---|---|---|---|
| Convex surface | 1,7 | 1,12 | 4,46 |
| Hollow surface | 1,9 | 0,75 | - |

## 4.6 XPS Analysis

XPS Analysis was conducted on sample 14 in a selected area with pits. Wide scan (Fig. 40) presents the main elements detected:

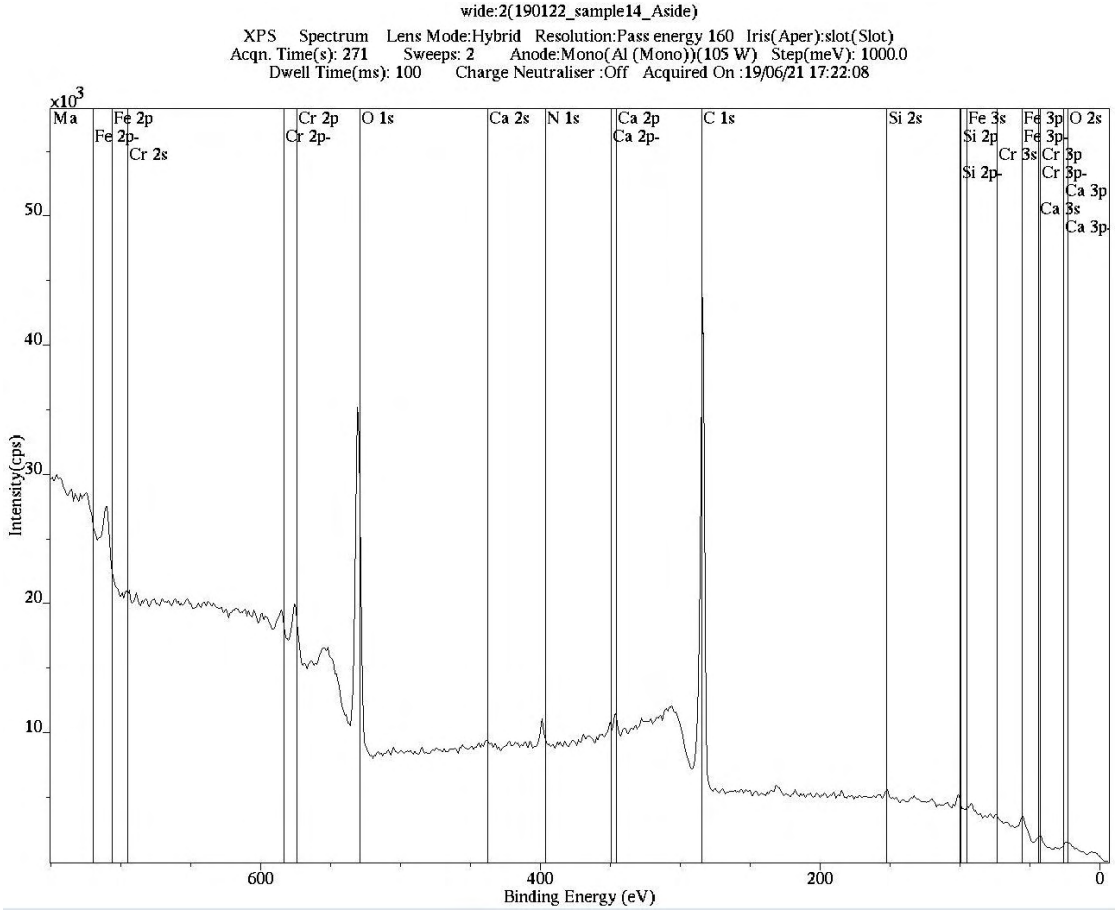


**Fig.40**: Wide scan spectrum

**Table 25**: Quantification report with contributions from carbon and oxygen

| Peak | Type | Position BE (eV) | FWHM (eV) | Raw Area (cps eV) | RSF | Atomic Mass | Atomic Conc % | Mass Conc % |
|---|---|---|---|---|---|---|---|---|
| C 1s | Reg | 284.633 | 1.297 | 5285.5 | 0.278 | 12.011 | 66.27 | 49.60 |
| O 1s | Reg | 531.383 | 3.499 | 5190.6 | 0.780 | 15.999 | 21.53 | 21.46 |
| Fe 2p | Reg | 710.383 | 3.484 | 23810.5 | 2.957 | 55.846 | 3.08 | 10.73 |
| Cr 2p | Reg | 576.233 | 3.261 | 18738.6 | 2.427 | 51.996 | 2.90 | 9.39 |
| N 1s | Reg | 399.683 | 1.911 | 3998.8 | 0.477 | 14.007 | 3.16 | 2.76 |
| Ca 2p | Reg | 347.433 | 1.888 | 4521.3 | 1.833 | 40.078 | 0.93 | 2.32 |
| Si 2p | Reg | 102.283 | 1.902 | 1904.1 | 0.328 | 28.086 | 2.13 | 3.73 |

**Table 16**: Quantification report - main elements (without contributions from carbon and oxygen)

| Peak | Type | Position BE (eV) | FWHM (eV) | Raw Area (cps eV) | RSF | Atomic Mass | Atomic Conc % | Mass Conc % |
|---|---|---|---|---|---|---|---|---|
| Fe 2p | Reg | 710.383 | 3.484 | 23810.5 | 2.957 | 55.846 | 25.27 | 37.09 |
| Cr 2p | Reg | 576.233 | 3.261 | 18738.6 | 2.427 | 51.996 | 23.75 | 32.45 |
| N 1s | Reg | 399.683 | 1.911 | 3998.8 | 0.477 | 14.007 | 25.89 | 9.53 |
| Ca 2p | Reg | 347.433 | 1.888 | 4521.3 | 1.833 | 40.078 | 7.63 | 8.05 |
| Si 2p | Reg | 102.283 | 1.902 | 1904.1 | 0.328 | 28.086 | 17.47 | 12.89 |

The deconvolution of the HR peaks from the *1s* orbital of C featured the typical adventitious Carbon contamination due to expose of the clear surface to the atmosphere. Namely C-C, CO-C and the O-C=O at 284.6, ~286 and ~288 eV [27] respectively (in all the binding energy values the error range is ±0.2eV). Supplementary, the *1s* orbitals of O confirmed the previous findings providing peaks at 531.3 and 532.5 eV for C-O and C=O bonds [28], while the peak at around 529.4eV corresponds to the binding energy of the metal oxides (mainly ferric oxides [29]). The results are remained identical with the clear surface analysis. [1]

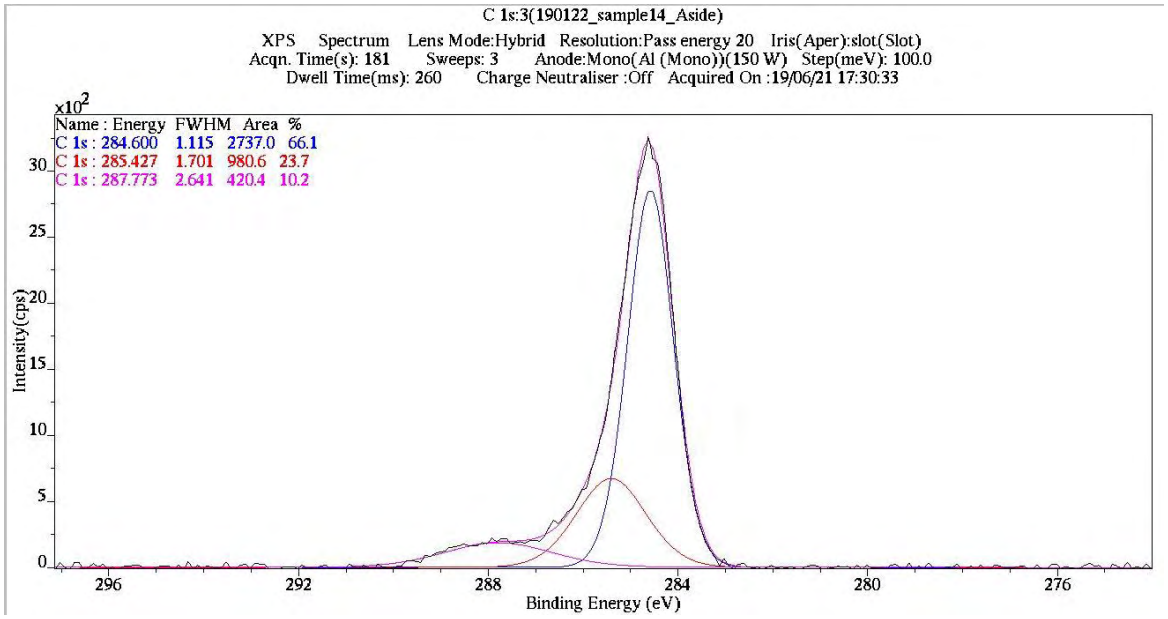


**Fig. 41**: C-1s peak deconvolution

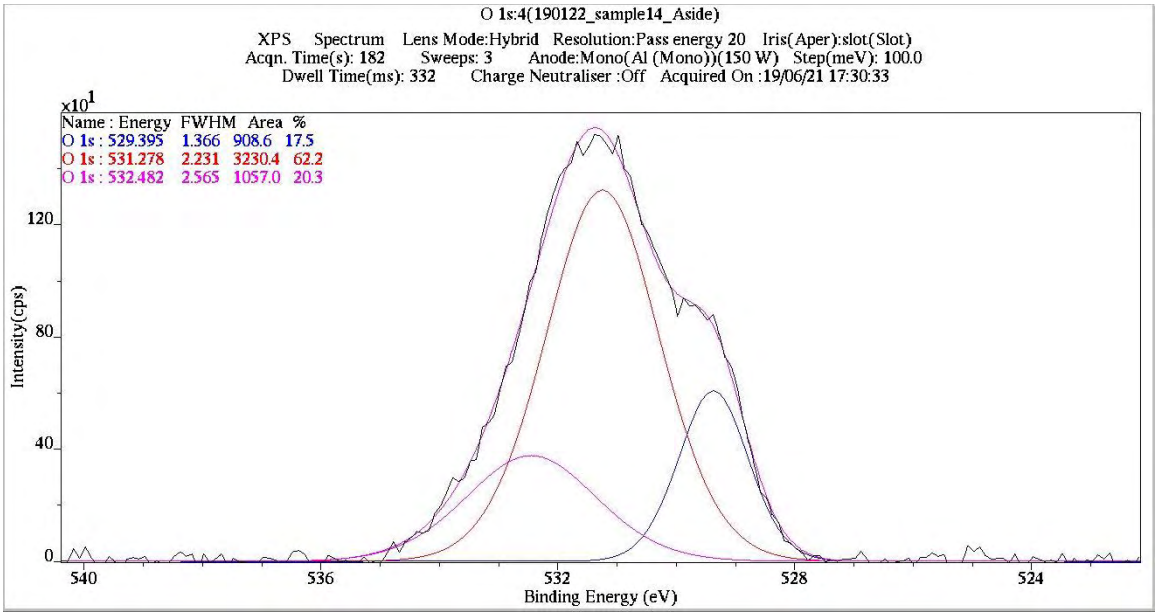


**Fig. 42**: O-1s HR peak deconvolution

The analysis of the Fe -*2p* peaks, revealed that the metal is oxidized, having two different oxidized states. The Fe -$2p_{3/2}$ orbital's peak position at 706.2 eV for the $Fe^0$ (metallic bonds) and at 710.5eV for the $Fe_2O_3$ compound. Oxidized/metallic ratio was calculated at about 8:1

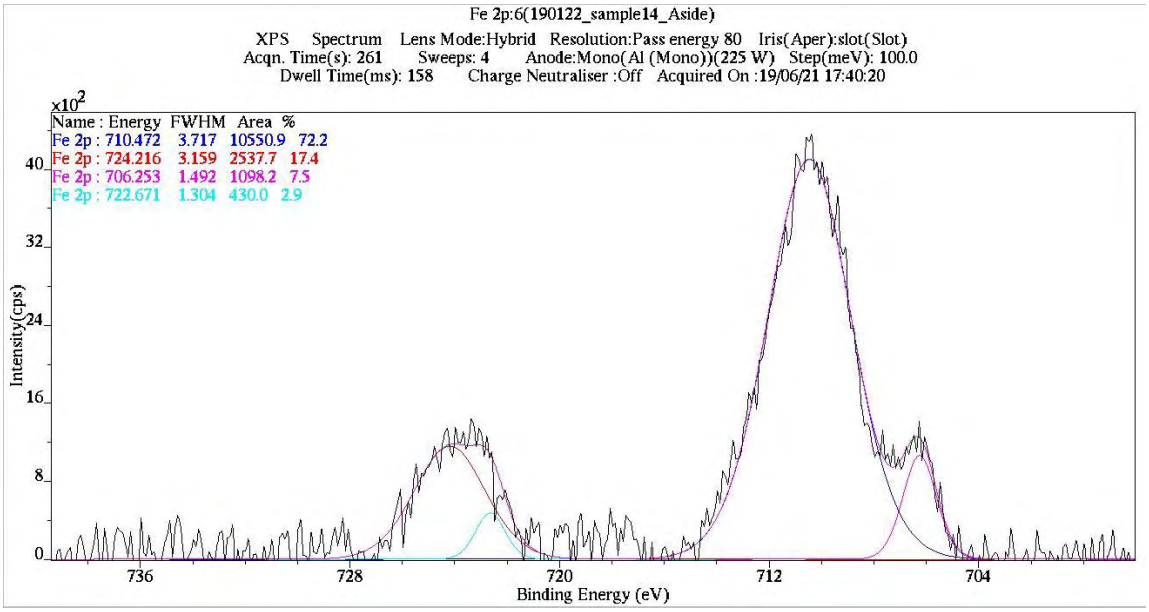


**Fig.43**: Fe-2p HR peak deconvolution

The Cr is found oxidized, too. $2p_{3/2}$ peak at 576.2eV for the $Cr_2O_3$ and a small contribution from metallic Cr (-$2p_{3/2}$ peak for $Cr^0$ at 573.1eV) [30–33]. Oxidized/metallic ratio around 9:1. The results are also remained identical with the clear surface analysis. [1]

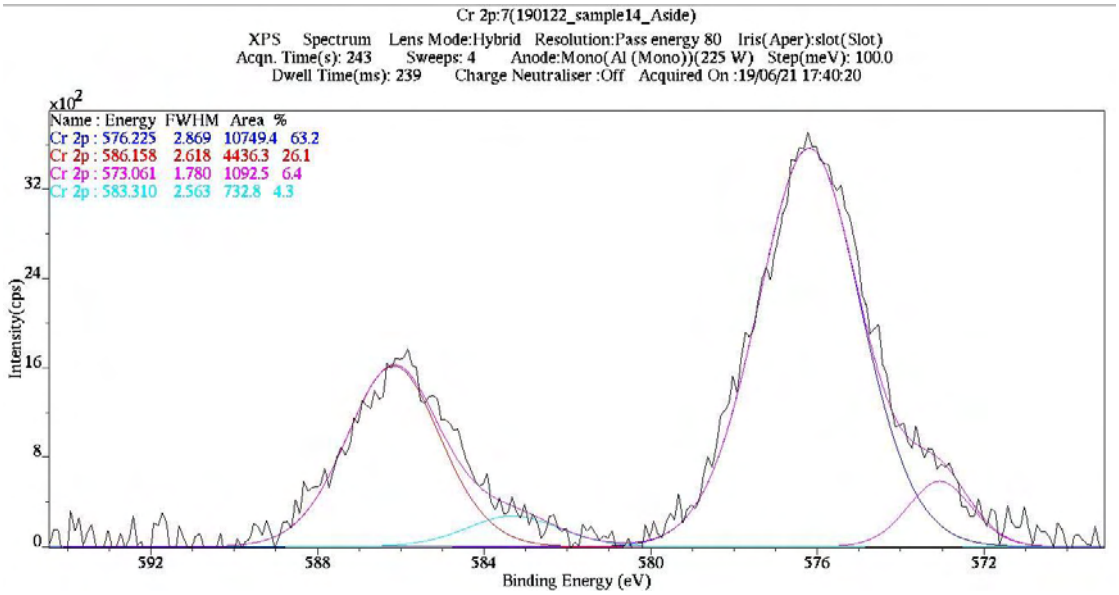


**Fig.44**: Cr-2p HR peak deconvolution.

Furthermore, N *-1s* orbital was centered at 399.9eV which is the characteristic B.E. for the $NSi_2O$ compound (N-Si bonds) [34]. The Si-N bonds conformed from the Si 2p orbitals [Si2p peak has closely spaced spin-orbit components ($\Delta$=0.63eV)], forming photoelectron peaks at ~102eV. The peak may include contributions from Si – C bonds, too [35].

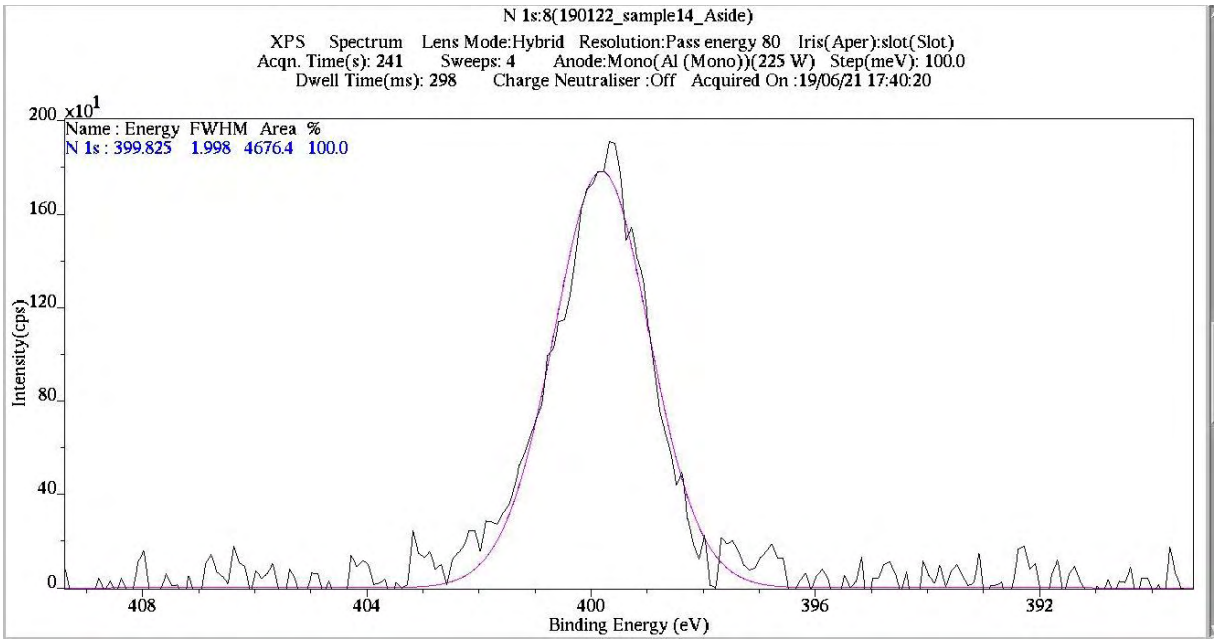


**Fig.45**: N-1s HR peak deconvolution.

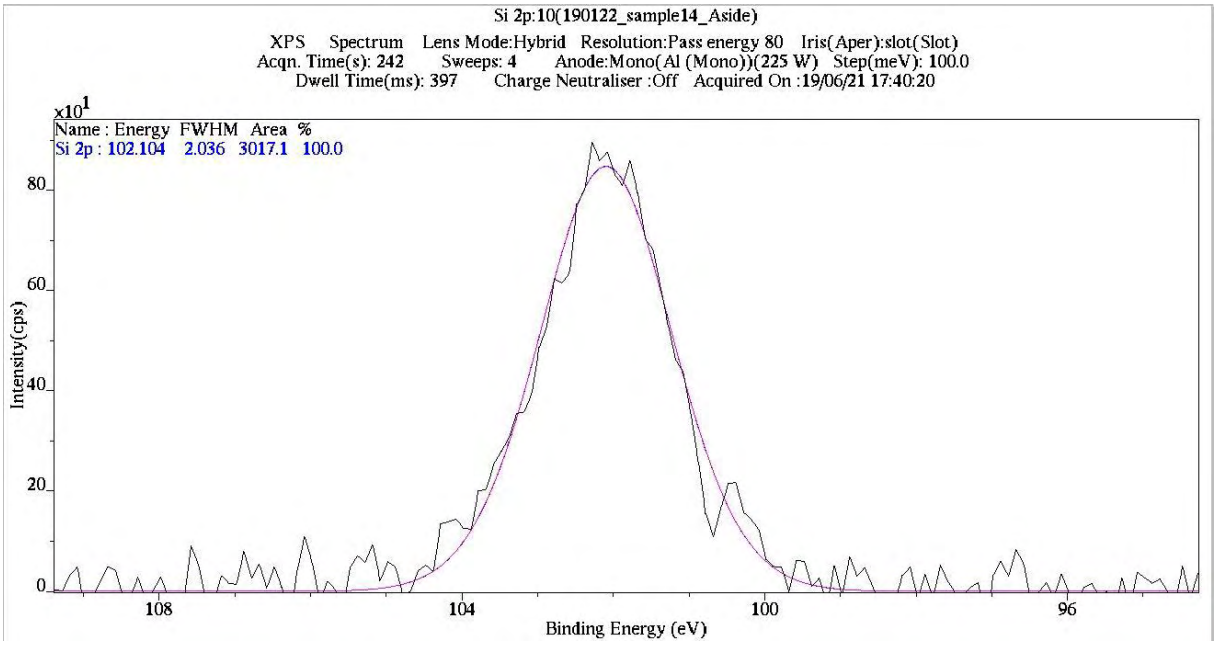


**Fig.46**: Si-2p HR peak deconvolution.

Finally, in this analysis surface region, the intensity from the Ca collected photoelectrons provided higher peak intensity (Fig. 47). Ca -$2p_{3/2}$ orbitals were recorded with binding energy at around 347.3eV, for the Ca-O bond and the $CaCO_3$ compound [36].

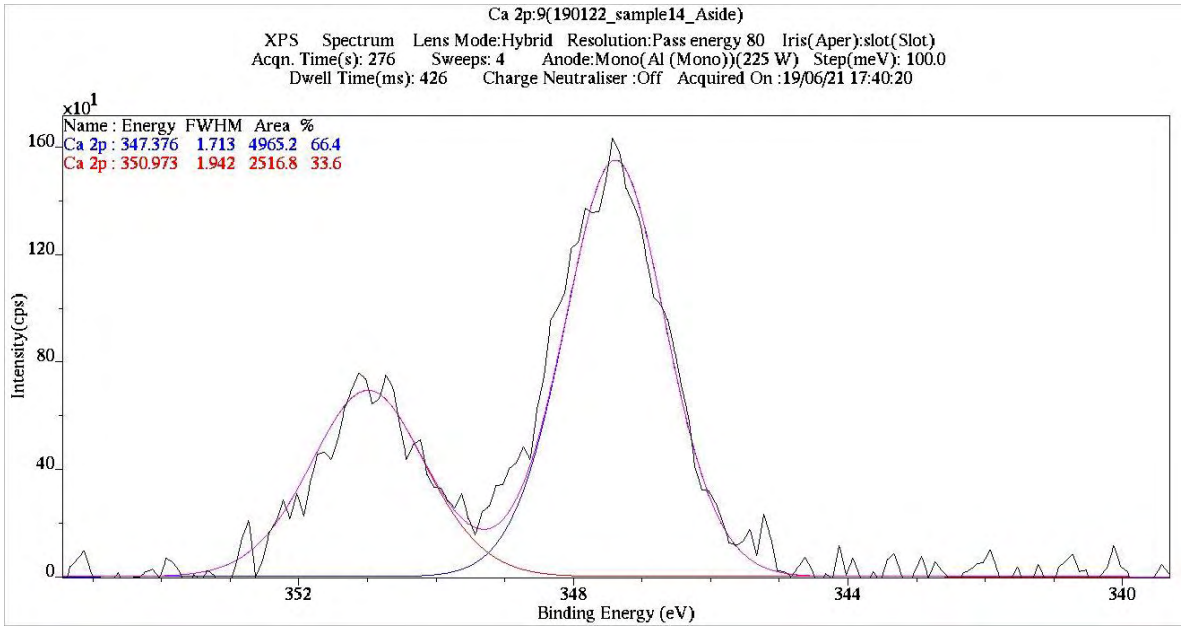


**Fig. 47**: Ca-2p HR peak deconvolution

## 4.8 Critical Pitting Temperature (CPT)

CPT test conducted on both the hollow and convex surfaces of the specimens. Fig. 48 shows the results of the CPT of 2707 using potentiostatic measurement under 1040 mV anodic potential at different temperatures in 5 wt.% NaCl solution.

Considering the criterion of 0.1 mA/cm$^2$ current density for the breakdown potential, the CPT of the HDSS 2707 for convex surfaces was 55 $^oC$ and for hollow surfaces 60 $^oC$ respectively.

Current density increases gradually indicating that the protective passive film starts to destabilize.

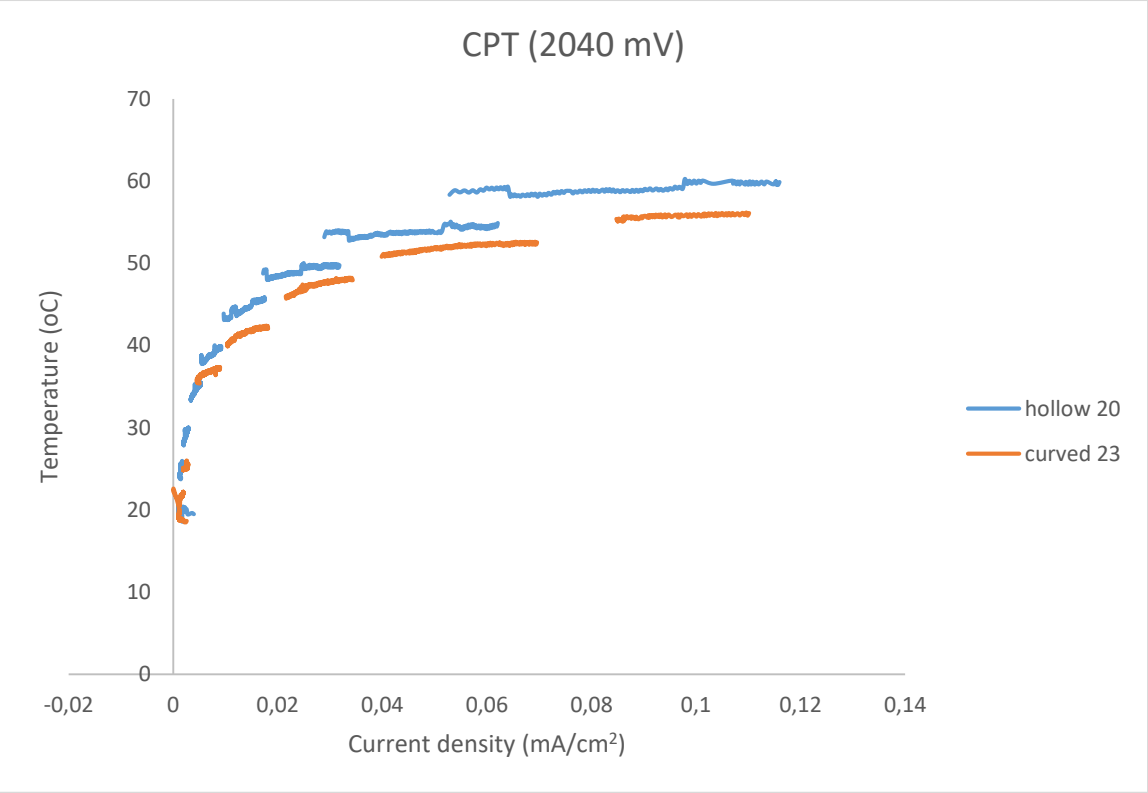


**Fig.48:** Potentiostatic polarization results of S32707 at 2040 mV/SCE in 5 wt.% NaCl solution.

# Chapter 5: Concluding remarks

## 5.1 Corrosion mechanism and products

Considering the results presented in Chapter 4 the main findings of this work can be summarized as follow:

- The polarization curves demonstrated the behavior of the specimen in 3.5 % NaCl. All the specimens are characterized by a region of oxidation (active stage) which is succeeded by the passivation stage. At the passivation stage, the passive film is formed. As the current density increases, the passivation stage is completed at a potential value, where the dissolution of the passive film occurs due to the attack of Cl ions.

- The stereoscopy examination determined the density and the size of the pits formed in the CCPT. Specimen 13 had greater corrosion resistance. Also, all the convex surfaces had lower pit density than the hollow due to the fact that convex surfaces had been polished before the CPP test. Salt deposits were found on the surface of all specimens.

- In addition, the microscopy examination determined the depth and shape of the pits. The deepest pit was around 14,756 μm (specimen 6). Furthermore, the different corrosion resistance of the ferrite and austenite was revealed. The ferrite phase seemed to be more prone to pitting corrosion as the PREN values of the two phases are different. This can be explained by the results of the AA and SEM where lower Cr values were detected.

- XPS analysis identified the products of corrosion. The analysis showed that on the surface there was carbon contamination and the metal has been oxidized. As for the Cr, it has been oxidized also and $Cr_2O_3$ and $Cr^0$ were formed. The oxidized/metallic ratio of Cr is around 9:1. The analysis of the Fe showed that $Fe_2O_3$ and metallic bonds were formed.

- The CPT was determined at 55 and 60 $^oC$ where the passive film starts to dissolve on convex and hollow surfaces respectively.

## 5.2. Comparison between the two different open circuit equilibrium times

Two different conditions of CPP tests have been conducted, one at 2 hours' open circuit equilibrium time [1] and the other one with 1-hour open circuit equilibrium time. Fig 49 contains all the relevant results, while Fig 50 and 51 contain the curves of the convex and hollows surface respectively. The following comments can be made:

- Active states ($E_{cp}$-$E_{corr}$) of the 1-hour open circuit equilibrium tests are smaller than the 2 hours' by almost 100 mV. Thus, the oxidation takes a lesser extent and the ability of passivation is higher at 1-hour tests' specimens.

- $E_{cp}$ and $i_{cp}$ values of the 1-hour equilibrium tests are lower than the 2 hours tests. Lower $i_{cp}$ means that the metal passivation is easier and lower $E_{cp}$ means that the protective film starts to form at lower potentials.

- $E_b$ is higher ~ 1000 mV from the $E_{cp}$, which is an indication of low pitting possibility. The breakdown potential at 2 hours open circuit equilibrium test began at lower potential and at this potential pits start to form.

- The difference between $E_b$ and $E_{corr}$ demonstrates the corrosion resistance. The lower the difference the higher the corrosion resistance. Specimens of the 1-hour open circuit equilibrium test shows greater corrosion resistance.

- The corrosion rate is expressed as penetration rate. The corrosion rates of 1-hour open circuit equilibrium test are 2 orders of magnitude smaller than those of 2-hours'. Thus, the depth of the pits is smaller (14 μm vs 38μm).

- Researchers observed a convex shape to the salt film at the bottom of the pits and new holes appearing around the pit mouth. They suggested that a change in film tightness may lead to different growth rates and pit shapes. This observation was explained by the varying distribution of chloride ions inside the pit, which changes the thickness of the salt film on the pit surface. The concentration of chloride ions is reduced at the edge of the pit, relative to its interior. Therefore, there is a rise in anodic current density at the edge of the pits, increasing the rate of dissolution and broadening the pit shape. [37] This can explain the differences in the shape of the pits. At the tests of 1-hour open circuit equilibrium time, more concentration of Cl ions inside the pits is detected by SEM analysis relative to the edge of the pit which create different shape of pits.

- As regards the quantity of Cr in the solutions after the cyclic polarization test. The Cr element is 0,1 ppm lower in the solution of 1-hour equilibrium time which shows that at this test the dissolution of the chromium surface film is lower.

**In conclusion:**

The specimens of the two CPP tests show differences on the morphology and depth of the pits that can be explained from the differences in the CPP curves, the stereo-optical observation, the AAS and SEM analysis. The corrosion mechanism according to the SEM analysis was the same. XPS analysis was identical except the N -1s orbital that was centered at much higher binding energy in comparison with the N-1s orbital of the specimen of the 2-hours equilibrium time.[1]

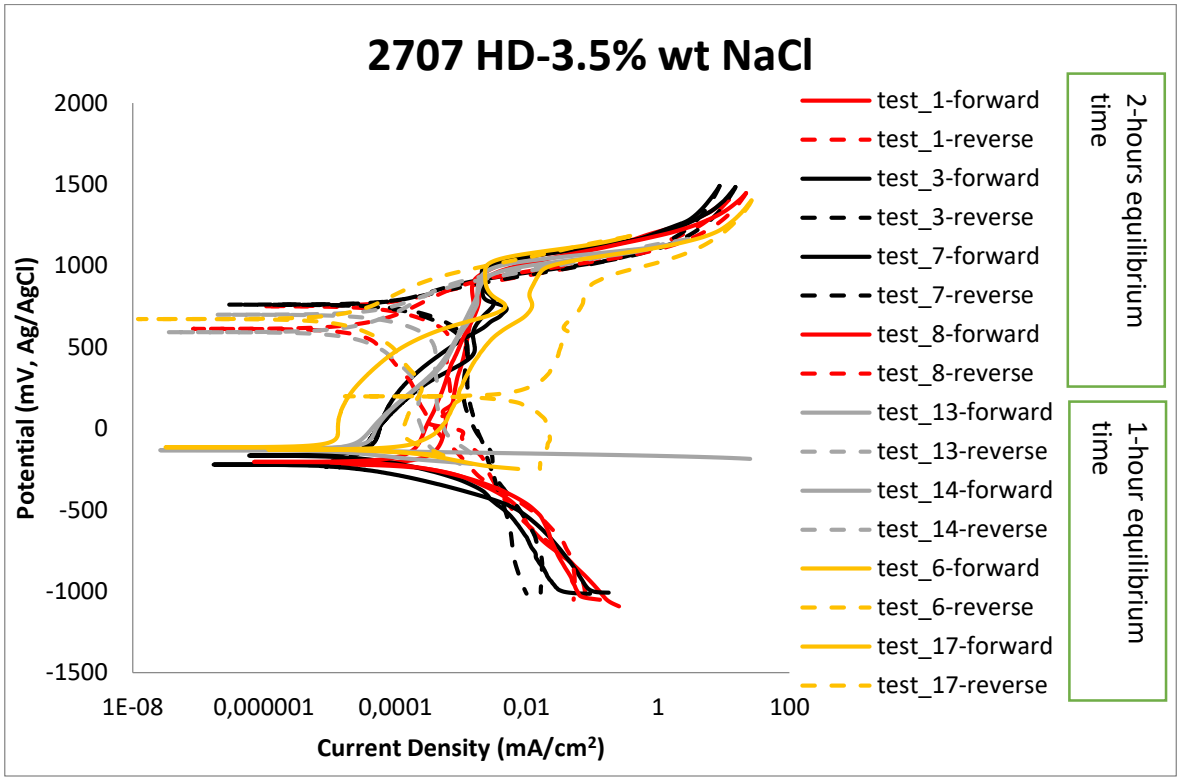


**Fig.49:** Cyclic Polarization curves at 1 and 2 hours' open circuit equilibrium time, test 1,8,13,14 referee to convex surfaces and test 3,7,6,17 to hollow.

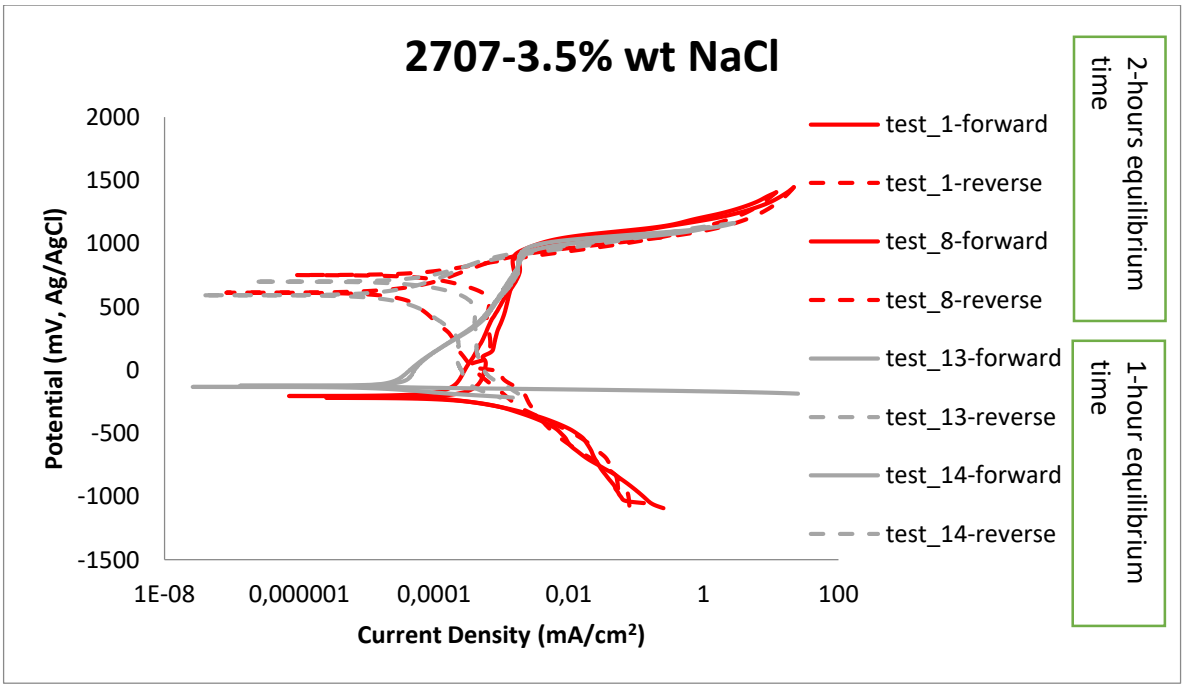


**Fig.50:** Cyclic Polarization curves of convex surfaces at 1 and 2 hours' open circuit equilibrium time

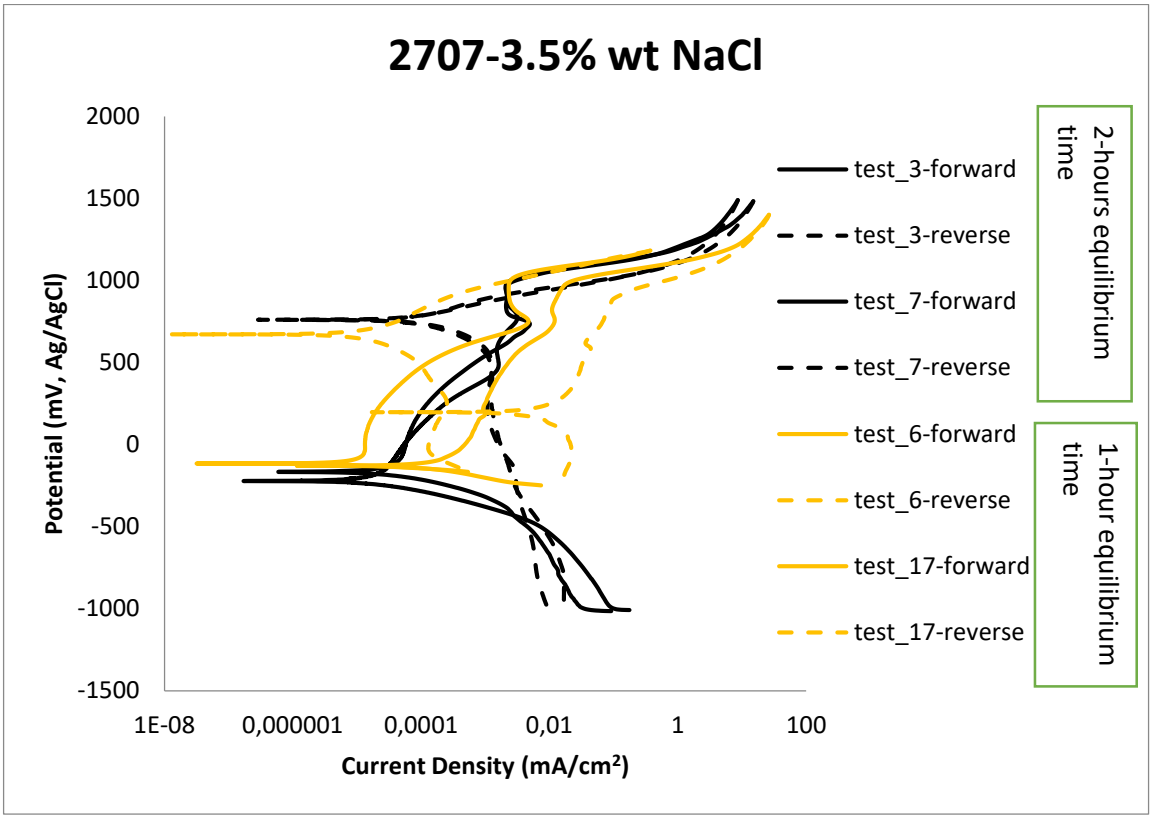


**Fig.51**: Cyclic Polarization curves of hollow surfaces at 1 and 2 hours' open circuit equilibrium time

## 5.3. Future Work Recommendations

Recommendations for future work are given below:

- Raman spectroscopy could be used for the in-depth characterization of the products formed during corrosion.
- Also, the conduction of cyclic potentiodynamic polarization test in temperatures higher than 25$^{o}$C could provide useful information for the material's behavior.
- One possible future study could investigate the pH. inside the pits and how it affects the propagation of pitting and the tightness of the protective film.
- Furthermore, the examination of the thickness and endurance of the protective passive film could provide more detailed information about the passivation ability of the steel. Also, conduction of cyclic potentiodynamic anodic polarization could provide more detailed information on the repassivation ability of the steel.

## References


[1] Corrosion performance of 2707 Hyper-Duplex Stainless Steel: Cyclic Potentiodynamic Polarization and microstructural characterization, Kleanthis Konstantinos Karagiannis,2018

[2] CORROSION AND CORROSION CONTROL an Introduction to Corrosion Science and Engineering,4th edition, R. Winston Revie, Harbert H. Uhlig, Wiley-interscience publication,2008.

[3] Mars G. Fontana, CORROSION ENGINEERING, Third Edition,1987.

[4] Potentiodynamic polarization studies of aluminum alloys in synthetic flue gas condensate, Lean Fong Khaw Lee,1986

[5] A. Lekatou, Corrosion and protection of metals in plain terms, Rethymno, Nimertis Editions, 2013

[6] Corrosion science and technology, David Talbot, James Tablot,2000

[7] Failure Analysis, cases studies from Greek industries, G. Haidemenopoulos, A. Zervaki,2018

[8] Investigation of Electrochemical Pitting Corrosion by Linear Sweep Voltammetry: A Fast and Robust Approach, Shashanka Rajendrachari

[9] Sato, N., The Stability of Localized Corrosion. Corrosion Science, 1995. 37(12): p. 1947-1967

[10] Standard Guide for Examination and Evaluation of Pitting Corrosion, ASTM, Designation: G 46-94, 2005

[11] Volume 13 Corrosion, ASM handbook

[12] Volume 13A Corrosion: Fundamentals, Testing, and Protection, ASM handbook

[13] Marina Knyazeva and Michael Pohl, Duplex Steels: Part I: Genesis, Formation, Structure,2013

[14] Jalal Alsarraf, Hydrogen Embrittlement Susceptibility of Super Duplex Stainless Steels,2010

[15] Sandvik duplex stainless steels, Sandvik Materials Technology, www.smt.sandvik.com

[16] Guocai Chai and Pasi Kangas, Sandvik white paper Hyper-duplex stainless steel

[17] Guocai Chai and Pasi Kangas, Super and hyper duplex stainless steels: structures, properties and applications,2016..

[18] Luca Brazzalotto, Microstructural transformations of different duplex stainless steels in advanced technological processes,2017

[19] Xiu-qing Xu, Mifeng Zhao, Yao-rong Feng, Fa-gen Li, Xiang ZhangA, Comparative Study of Critical Pitting Temperature (CPT) of Super Duplex Stainless Steel S32707 in NaCl Solution,2018

[20] Standard Reference Test Method for Making Potentiostatic and Potentiodynamic Anodic Polarization Measurements, ASTM G5 - 94(2004)

[21] Standard Test Method for Conducting Cyclic Potentiodynamic Polarization Measurements for Localized Corrosion Susceptibility of Iron-, Nickel-, or Cobalt-Based Alloys, ASTM G61 - 86(2014)

[22] ASTM G71-81(2014) Standard Guide for Conducting and Evaluating Galvanic Corrosion Tests in Electrolytes

[23] Standard Practices for Detecting Susceptibility to Intergranular Attack in Austenitic Stainless Steels ASTM A262(2015)

[24] Ευαγγελία Ευθ. Γκόλια. 2003. Ρύπανση Εδαφών της Θεσσαλίας από Βαρέα Μέταλλα (Zn, Cu, Mn, Fe, Cd και Pb) και πρόσληψη αυτών από ποικιλίες καπνού. Απεικόνιση της χωρικής παραλλακτικότητας των βαρέων μετάλλων σε επιλεγμένες περιοχές της μελέτης. Διδακτορική Διατριβή. Πανεπιστήμιο Θεσσαλίας. Βόλος.

[25] Vesna Alar, Ivan Stojanović, Bruno Židov, Franjo Ivušić, Corrosion Resistance of Highly Alloyed Materials in 3.5% NaCl Solution at Elevated Temperature,2013

[26] Standard Test Method for Electrochemical Critical Pitting Temperature Testing of Stainless Steels1,ASTM G150-99

[27] https://xpssimplified.com/elements/carbon.php

[28] https://xpssimplified.com/elements/oxygen.php

[29] T. Zhang, X. Meng, Z. He, Y. Lin, X. Liu, D. Li, J. Li, X. Qiu, Preparation of Magnetic Nanoparticles via a Chemically Induced Transition: Role of Treating Solution's Temperature, Nanomaterials. 7 (2017) 220. doi:10.3390/nano7080220.

[30] M. Naffati, S. Zanna, P. Cornette, D. Costa, P. Marcus, M.M. Abderrabba, S. Somrani, Adsorption of phenyl phosphate on Ni-Cr alloy surface: Experimental and theoretical investigations, Phosphorus. Sulfur. Silicon Relat. Elem. 193 (2018) 185–191. doi:10.1080/10426507.2017.1395877.

[31] M. Aronniemi, J. Sainio, J. Lahtinen, Chemical state quantification of iron and chromium oxides using XPS: the effect of the background subtraction method, Surf. Sci. 578 (2005) 108–123. doi:10.1016/j.susc.2005.01.019.

[32] N. Gunasekaran, Surface characterization and catalytic properties of perovskite type solid oxide solutions, La0.8Sr0.2BO3 (B = Cr, Mn, Fe, Co or Y), Solid State Ionics. 83 (1996) 145–150. doi:10.1016/0167-2738(95)00232-4.

[33] E. Pecheva, L. Pramatarova, Modified Inorganic Surfaces as a Model for Hydroxyapatite Growth, Trans Tech Publications Ltd Brandrain 6 CH-8707 Uetikon-Zuerich Switzerland., 2006.

[34] https://xpssimplified.com/elements/nitrogen.php

[35] https://xpssimplified.com/elements/silicon.php

[36] https://xpssimplified.com/elements/calcium.php

[37] Fahd A. Almuaili, Characterization of 3D pitting corrosion kinetics of stainless steel in chloride containing environments ,2017

[38] Y.X. Qiaoa, Y.G. Zhenga, P.C. Okafor, W. Kea, Electrochemical behavior of high nitrogen bearing stainless steel,in acidic chloride solution: Effects of oxygen, acid concentration and surface roughness, 2009.